

High sensitivity of tropical precipitation to local sea-surface temperature

Article

Accepted Version

Good, P., Chadwick, R., Holloway, C. E. ORCID:
<https://orcid.org/0000-0001-9903-8989>, Kennedy, J., Lowe, J.
A., Roehrig, R. and Rushley, S. S. (2020) High sensitivity of
tropical precipitation to local sea-surface temperature. *Nature*,
589 (7842). pp. 408-414. ISSN 0028-0836 doi:
<https://doi.org/10.1038/s41586-020-2887-3> Available at
<http://centaur.reading.ac.uk/93705/>

It is advisable to refer to the publisher's version if you intend to cite from the work. See [Guidance on citing](#).

Published version at: <https://www.nature.com/articles/s41586-020-2887-3>

To link to this article DOI: <http://dx.doi.org/10.1038/s41586-020-2887-3>

Publisher: Nature Publishing Group

All outputs in CentAUR are protected by Intellectual Property Rights law, including copyright law. Copyright and IPR is retained by the creators or other copyright holders. Terms and conditions for use of this material are defined in the [End User Agreement](#).

www.reading.ac.uk/centaur

CentAUR

Central Archive at the University of Reading

Reading's research outputs online

1 **High sensitivity of tropical precipitation to local sea-surface**
2 **temperature**

3

4 Peter Good^{1*}, Robin Chadwick^{1,2}, Christopher E. Holloway³, John Kennedy¹, Jason A.
5 Lowe^{1,4}, Romain Roehrig⁵, Stephanie S. Rushley⁶

6

7 ¹MetOffice Hadley Centre, Exeter, United Kingdom.

8 ²Global Systems Institute, University of Exeter.

9 ³Department of Meteorology, University of Reading, Reading, United Kingdom.

10 ⁴Priestley International Centre for Climate, University of Leeds, United Kingdom.

11 ⁵CNRM, Université de Toulouse, Météo-France, CNRS, Toulouse, France

12 ⁶Department of Atmospheric Sciences, University of Washington, Seattle, Washington
13 98195, USA.

14

15

16 **Abstract**

17

18 Precipitation and atmospheric circulation are the coupled processes through which tropical
19 ocean surface temperatures drive global weather and climate¹⁻⁵. Local ocean surface
20 warming tends to increase precipitation, but this local control is hard to disentangle from

21 remote effects of conditions elsewhere. Such remote effects occur, for example, from El
22 Niño Southern Oscillation (ENSO) events in the equatorial Pacific, which alter precipitation
23 across the tropics. Atmospheric circulations associated with tropical precipitation are
24 predominantly deep, extending up to the tropopause. Shallow atmospheric circulations^{6–8},
25 impacting the lower troposphere, also occur, but the importance of their interaction with
26 precipitation is unclear. Uncertainty in precipitation observations^{9,10}, and limited
27 observations of shallow circulations¹¹, further obstruct understanding of the ocean’s influence
28 on weather and climate. Despite decades of research, persistent biases remain in many
29 numerical model simulations^{12–18}, including excessively-wide tropical rainbands^{14,18}, the
30 ‘double-intertropical convergence zone (ITCZ) problem’^{12,16,17} and too-weak responses to
31 ENSO¹⁵. These demonstrate stubborn gaps in our understanding, reducing confidence in
32 forecasts and projections. Here we show that the real world has a high sensitivity of seasonal
33 tropical precipitation to local sea-surface temperature. Our best observational estimate is
34 80% precipitation change per g/kg change in the saturation specific humidity (itself a
35 function of the ocean surface temperature). This observed sensitivity is higher than in 43 of
36 the 47 climate models studied, and is associated with strong shallow circulations. Models
37 with more realistic sensitivity have smaller biases across a wide range of metrics. Our results
38 apply to both temporal and spatial variation, over regions where climatological precipitation
39 is around 1 mm/day or greater. Novel analysis of multiple independent observations, physical
40 constraints and model data, underpin these findings. The spread in model behaviour is further
41 linked to differences in shallow convection, providing a focus for accelerated research, to
42 improve seasonal forecasts through multidecadal climate projections.

43

44

45 Main paper

46

47 We first define a measure (k_{qsat}) of the sensitivity of seasonal mean precipitation to variation
48 in local sea surface temperature (SST). We will show that k_{qsat} is a key property of the
49 atmosphere, using it to link diverse gaps in understanding to a limited subset of physical
50 mechanisms. Precipitation increases non-linearly with SST¹⁹. Since tropical precipitation
51 increases roughly exponentially with column atmospheric water vapour^{20,21}; and over
52 seasonal or longer timescales, SST variation forces variation in column water vapour²², via
53 differences in saturation specific humidity of the ocean surface (q_{sat} , Methods), we define k_{qsat}
54 as follows:

$$55 \log_e(P_1/P_0) \approx k_{\text{qsat}} * (q_{\text{sat},1} - q_{\text{sat},0}) + \langle \text{other processes} \rangle \quad \text{Equation 1.}$$

56 This describes the variation in precipitation (from P_0 to P_1) driven by local variation in q_{sat}
57 (from $q_{\text{sat},0}$ to $q_{\text{sat},1}$). This approximation is validated within the calculation of k_{qsat} (Methods).
58 Moist static energy arguments¹⁹ also predict a roughly exponential relationship between q_{sat}
59 and P . k_{qsat} quantifies the combined effect of the physical processes by which local SST
60 anomalies affect precipitation at the same location. The 'other processes' term includes the
61 effects of internal atmospheric variability independent of SST, and of remote forcing from
62 land or SST elsewhere, which can be large at individual locations or times. In order to
63 estimate k_{qsat} , we filter out these other processes, by combining information from multiple
64 locations and times (see Methods). We evaluate k_{qsat} from interannual variability, with P_0
65 and $q_{\text{sat},0}$ taken as seasonal climatological means at each location for each season. However,
66 our estimates of k_{qsat} are shown to be also informative about spatial variations in
67 precipitation.

68

69 k_{qsat} relates most directly to the strength of percentage variations in precipitation. Writing
70 Equation 1 in exponential form, percentage precipitation differences are a function of k_{qsat}
71 and q_{sat} :

$$72 \quad (P_1 - P_0)/P_0 * 100 \approx 100 [\exp(k_{\text{qsat}} * (q_{\text{sat}} - q_{\text{sat},0})) - 1]. \quad \text{Equation 2}$$

73 Absolute differences depend also on the reference precipitation P_0 :

$$74 \quad P_1 - P_0 \approx P_0[(\exp(k_{\text{qsat}} * (q_{\text{sat}} - q_{\text{sat},0})) - 1)], \quad \text{Equation 3}$$

75 (in absolute terms, precipitation variations are largest in regions of large mean precipitation¹⁹).

76 However, we will show that spatial variation in P_0 itself also depends partly on k_{qsat} .

77

78 **Validating satellite observations**

79 Given uncertainty in precipitation observations^{9,10}, we perform a high-precision evaluation of
80 $\log(\text{precipitation})$ (as Equation 1) from two satellite datasets: TRMM^{23,24} (3B43, v7) and
81 GPCP²⁵ (v2.3), both for 1998-2015. We do this (Methods) using in-situ raingauge data from
82 89 buoys of the Global Tropical Moored Buoy Array (GT MBA)²⁶⁻²⁸. Satellite-GT MBA
83 validation is challenging: on top of satellite error^{9,10}, the GT MBA point observations include
84 noise from small-scale variability unresolved by satellite data, missing data, error in
85 individual raingauges and wind undercatch²⁹. Our method reduces this noise considerably,
86 giving a tight relationship between GT MBA and TRMM data (Figure 1a). Critically, the best
87 fit gradient ≈ 1 , so TRMM accurately retrieves differences in \log precipitation. On the other
88 hand, GPCP underestimates differences in \log precipitation (Figure 1b, gradient > 1 ;
89 differences between TRMM and GPCP emerge primarily at low precipitation⁹), although
90 GPCP is more suitable over larger spatial scales (Extended data Figure 1). Since TRMM
91 captures differences in $\log(\text{precipitation})$ more accurately than GPCP, TRMM is used below.

92

93 **Model precipitation simulations**

94 We first highlight precipitation biases in 28 atmospheric models from the fifth Coupled
95 Model Intercomparison Project (Methods), each forced by observed SST (CMIP5 AMIP
96 experiment; Figure 2a-f). We quantify temporal, seasonal and spatial variation in
97 precipitation: the 1997-98 El Niño divided by the mean of the 1998-2000 La Niñas; Aug-Oct
98 divided by Feb-Mar seasons, and precipitation scaled by its latitudinal maximum. Our
99 metrics coincide with significant spatial or temporal differences in SST (Methods). Spatial
100 variation across the west Pacific is excluded, for example, because spatial gradients in SST
101 are weak there, so model differences in k_{qsat} will be less important for spatial variation there.
102 Given the form of Equation 1, precipitation is shown on log scales as ratios. Although some
103 models are close to the observations, in others, biases exceed a factor of five in the El
104 Niño/La Niña ratio, seasonal cycles over the Atlantic and West Pacific, and in the Atlantic
105 spatial pattern for the Aug-Oct season (Figure 2a-d). Biases over a factor of two occur in the
106 spatial patterns of the East Pacific annual mean (the long-standing ‘double-ITCZ’
107 problem^{12,17}) and the Indian Ocean for November-April (Figure 2e-f). Such biases are
108 known, but their causes are not well understood.

109

110 These biases (Figure 2a-f) all correspond to excessively weak spatial/temporal variations in
111 precipitation (precipitation ratios too close to 1; including excessively-wide inter-tropical
112 convergence zones^{14,18}). This suggests a hypothesis (H_0), that the sensitivity of seasonal
113 precipitation to local SST (k_{qsat}) may be too weak in many models.

114

115 To test H_0 objectively, we use a method independent of Figure 2 (Figure 2 was used to
116 propose H_0). This involves estimating k_{qsat} for each model using different data.

117

118 **Evaluating k_{qsat} in models**

119 We evaluate k_{qsat} using interannual variability in seasonal mean precipitation and SST (the
120 AMIP SST dataset³⁰ used to drive the model experiments; using years 1980-2005). k_{qsat} is
121 calculated using gridpoint values of seasonal precipitation and q_{sat} , from each location in the
122 study region, and for each year. With these data, Equation 1 becomes a model of the effect of
123 local interannual SST variability on precipitation:

$$124 \log_e(P(x,t)/P_0(x)) \approx k_{qsat} * (q_{sat}(x,t) - q_{sat,0}(x)) + \langle \text{other processes} \rangle,$$

125 where (x,t) indicates values for each gridpoint and year; and here, P_0 and $q_{sat,0}$ are the
126 corresponding climatological means for each gridpoint. We estimate k_{qsat} from these data
127 using a modified regression approach (detailed in Methods), minimising the influence of
128 other processes in Equation 1.

129

130 To minimise observational error, we exclude the 30% of the tropical oceans with the lowest
131 climatological mean SST (Figure 3b-e, area outside white contour).

132

133 Taking logarithms means that all areas of our study region contribute relatively equally to our
134 k_{qsat} estimate (Methods). Consequently, k_{qsat} is relevant over most of the tropical oceans
135 (Figure 3a, correlations are high except for the left bar). k_{qsat} is inapplicable over the coolest,

136 driest ocean regions (Figure 3a, left bar; area masked in Figure 3b-e). The applicable region
137 corresponds to climatological precipitation $> \sim 1$ mm/day (Figure 3b-e, orange contour).

138

139 k_{qsat} is intended to be independent of large-scale SST spatial patterns. To avoid bias from the
140 large, recurrent ENSO pattern, our ‘sortav’ regression method first processes the data so all
141 years contribute equally. Linear regression is then applied to obtain k_{qsat} . Rankings of
142 CMIP5 models by k_{qsat} are robust: insensitive to season, to using fewer years of data, or to
143 excluding ENSO years - Extended data Figure 2e-g. Calculated this way, k_{qsat} is less
144 sensitive to the time period used than with simple least squares regression (Extended Data
145 Figures 2h, 7).

146

147 We find that the sensitivity of precipitation to local SST variability is much stronger in some
148 models than in others: k_{qsat} varies across CMIP5 models by a factor of 2.5 (0.26-0.66 kg/g;
149 median = 0.46). We group the models into ‘high- k_{qsat} ’ (the 6 models with the largest k_{qsat}
150 values), ‘low- k_{qsat} ’ (the lowest 6 k_{qsat} values) and ‘mid-range’ subsets.

151

152 In Equation 2, setting $(q_{sat} - q_{sat,0})$ to 1, expresses k_{qsat} as the percentage precipitation change
153 per g/kg change in saturation specific humidity (q_{sat}):

154

$$155 \quad (P_1 - P_0)/P_0 * 100 \approx 100 [\exp(k_{qsat} * 1) - 1] = 100 [\exp(k_{qsat}) - 1]. \quad \text{Equation 4}$$

156

157 Expressed this way, the precipitation sensitivity in CMIP5 models spans 30-93% per g/kg
158 (median = 58%). For context, q_{sat} can vary by a few g/kg, 10° either side of the East Pacific
159 ITCZ during Aug-Oct, and anomalies during ENSO events have a similar magnitude.

160

161 **High sensitivity of precipitation to SST**

162 We hypothesised above (H_0) that k_{qsat} may be too low in most models. To begin testing this,
163 the results in Figure 2a-f are replotted, but with the 'high- k_{qsat} ' subset of models highlighted in
164 magenta (Figure 2g-l). The 'high- k_{qsat} ' subset shows much better agreement with TRMM than
165 the full ensemble, in all six panels. Conversely, the 'low- k_{qsat} ' subset performs much worse
166 (Extended data Figure 3). Next, we calculate $k_{\text{qsat}}^{(\text{spatial})}$ (Methods): as k_{qsat} , but using spatial
167 patterns in climate means, rather than internal variability (Figure 4b). Again, models closest
168 to the observations (Figure 4b, horizontal line) tend to be those with high k_{qsat} . These results
169 all imply that k_{qsat} should be high in the real world (H_0).

170

171 These results also show that k_{qsat} is relevant to both spatial and temporal variations in
172 precipitation. We emphasise this by quantifying the overall sensitivity of precipitation to
173 local SST ($k_{\text{qsat}}^{\text{spattemp}}$), including both spatial and temporal variations (including spatial
174 variation in P_0 , Methods). $k_{\text{qsat}}^{\text{spattemp}}$ is well correlated with k_{qsat} (Extended data Figure 2i).
175 This confirms that k_{qsat} is a useful measure of the underlying sensitivity of precipitation to
176 local SST, relevant to spatial and temporal variations. k_{qsat} does not give information about
177 tropical mean precipitation, which is governed by different processes³¹. k_{qsat} remains our
178 primary measure of precipitation sensitivity to local SST, because it is insensitive to details of
179 SST patterns. In contrast, $k_{\text{qsat}}^{\text{spattemp}}$ and $k_{\text{qsat}}^{(\text{spatial})}$ may be sensitive to the specific spatial

180 patterns in climatological SST (Methods), explaining some of the noise in Figure 4b and
181 Extended data Figure 2i.

182

183 We estimate a lower bound for k_{qsat} , using observed interannual variability (independent of
184 Figure 2; Methods). Three values of k_{qsat} are estimated, exactly as for the models, but using
185 TRMM precipitation, and q_{sat} from each of three different SST datasets (HadISST³² version
186 1.1, ERSST³³ version 4 and COBE³⁴ version 2). Uncertainties are estimated, from SST error
187 (including regression dilution bias) and internal variability (the TRMM observational period
188 only partly overlaps the model simulation period). A lower observational bound (95%
189 confidence) of 0.51 kg/g for k_{qsat} is obtained.

190

191 For a central observational estimate of k_{qsat} (details in Methods), we return to Figure 2. We
192 ask: if all CMIP5 models had the same value of k_{qsat} , with what value would they best
193 reproduce the observations in Figure 2? We first find where, geographically, the models are
194 most sensitive to k_{qsat} . This reveals seven intervals (shaded in Figure 2g-l). For each interval,
195 model errors relative to TRMM are regressed against modelled k_{qsat} (Extended data Figure 6).
196 For each interval, k_{qsat} is estimated as where the regression line intercepts the x-axis (the
197 value for a theoretical model with zero precipitation error). These seven estimates of k_{qsat}
198 range from 0.56 to 0.68 kg/g (Figure 4a, white dashed lines), all larger than our lower bound
199 estimate. The spread of estimates comes from uncertainty in processes not quantified by
200 k_{qsat} . The range of conditions used, covering spatial, seasonal and temporal variability across
201 different locations, helps to quantify and mitigate this uncertainty. Robustness is tested by
202 plotting results from the sixth model intercomparison project (CMIP6, not used to select the
203 seven intervals) on Extended data Figure 6. The mean of the seven k_{qsat} values (0.6 kg/g; or,

204 using Equation 4, 80% per g/kg) is our central estimate (for 1980-2005; other periods would
205 give slightly different values, from internal SST variability - Extended data Figure 2h).

206

207 These results, from two independent methods, suggest that most models underestimate k_{qsat} .
208 Our central estimate (0.6 kg/g, Figure 4a, horizontal black line; Figure 4b, vertical line) is
209 greater than 43 of the 47 model values from CMIP5 and CMIP6. This implies that models
210 underestimating the sensitivity of precipitation to local SST underlies a range of model biases
211 over tropical oceans. CMIP5 and CMIP6 have similar ranges of k_{qsat} values (Figure 4a),
212 highlighting the need for accelerated model development.

213

214 Other studies³⁵ have found biases in a different aspect of the SST-precipitation relationship:
215 model precipitation often tracks SST maxima more closely than in observations. We quantify
216 this in each CMIP5 model as the correlation coefficient between climatological spatial
217 patterns of precipitation and SST, for each season, then average the four seasonal values.
218 This ‘spatial-correlation index’ is uncorrelated with k_{qsat} ($r = 0.01$; i.e. models with a high
219 spatial-correlation index can have high, low or intermediate k_{qsat}), so it involves different
220 processes.

221

222 **Processes behind uncertainty in k_{qsat}**

223 To guide model improvements, we explore what causes model differences in k_{qsat} , revealing
224 links to shallow atmospheric circulations. We first note that k_{qsat} involves processes
225 unrelated to tropical mean precipitation: the correlation across CMIP5 models between the

226 two measures is 0.03. Energy budgets constrain tropical mean precipitation³¹, while the value
227 of k_{qsat} affects precipitation variation in both time and space.

228

229 Beginning with interannual variability, we define $k_{\text{qsat}}^{\text{wap}}(p)$: the sensitivity of the vertical
230 pressure velocity (wap) to local SST change, at each pressure level (p). This is evaluated like
231 k_{qsat} , using data from all seasons across the tropical oceans, but using wap(p) instead of
232 log(precipitation). A deep mode dominates tropical variability³⁶, so the CMIP5 mean profile
233 of $k_{\text{qsat}}^{\text{wap}}$ peaks around 450 hPa (Figure 5a). In contrast, model spread in k_{qsat} is linked to
234 shallow circulations: correlations between $k_{\text{qsat}}^{\text{wap}}(p)$ and k_{qsat} (Figure 5b) peak near 700hPa (r
235 = -0.9; correlations are small at 1000hPa, as wap approaches zero near the surface). That is,
236 in models with high k_{qsat} (as in the real world), shallow circulations respond strongly to SST
237 anomalies. Although deep circulations are important³⁶ in all models, and shallow circulations
238 have been linked to mean precipitation, especially over the Eastern Pacific⁷, our novel finding
239 is that shallow circulations are central to model uncertainty in SST-driven precipitation
240 variability, across the tropics.

241

242 Shallow circulations are further linked to model differences in climate means. We study
243 zonal, ocean-only means over 180W-10E (most of the Pacific, entire Atlantic), in Aug-Oct,
244 when meridional SST gradients are strong. CMIP5 results are used to define key regions
245 (black and orange lines in Figure 5c-e), and CMIP6 used to test the conclusions. As
246 expected^{4,7}, CMIP5 mean vertical velocity profiles are bottom heavy, but extend throughout
247 the troposphere (Figure 5c, colours). Meridional wind (white contours) peaks near the
248 tropopause, with a weaker shallow flow between 500-700hPa³⁷. Again, however, inter-model
249 spread in k_{qsat} is associated with shallow circulations: models with high k_{qsat} have stronger

250 shallow descent south of the ITCZ between 600-850hPa (Figure 5d, yellow; Extended Data
251 Figure 8a, magenta line; Extended Data Figure 8d). They also tend to have stronger shallow
252 ascent in the ITCZ (Figure 5d, blue region; Extended Data Figure 8c, magenta line), stronger
253 trade winds and stronger return flow between 500-700hPa (Figure 5d, white contours;
254 Extended Data Figure 8b, magenta line). This shallow circulation is weak in the low- k_{qsat}
255 mean (Extended Data Figure 8a-c, blue lines).

256

257 The weak link between model differences in k_{qsat} and deep circulations may arise partly from
258 physical constraints. In descending air, differences in vertical velocity are largest below
259 about 600 hPa (Extended Data Figure 8a,i). This is partly explained by the vertically-
260 integrated dry static energy (DSE) budget. This budget constrains vertical velocities,
261 requiring balance between radiative, sensible and latent heating, and advection of DSE
262 (Methods). In descending air above 600 hPa, there are fewer uncertain processes affecting
263 this budget, with negligible energy input from cloud and precipitation. Here, therefore,
264 downward advection of DSE is balanced mostly by dry clear-sky radiative cooling (Extended
265 Data Table 1). Further, vertical temperature profiles are similar across CMIP5 models. This
266 constrains both radiative cooling and vertical gradients of DSE, limiting model differences in
267 vertical velocity. Model temperatures are constrained, near the surface by SST, and near the
268 tropopause as modelling groups aim to reproduce observed outgoing longwave radiation.
269 Below 600hPa, there are additional sources of uncertainty, from cloud and precipitation³⁸,
270 leading to larger model differences in shallow descent, and so stronger links to differences in
271 k_{qsat} .

272

273 The depth of the meridional return flow (500-700hPa, Figure 5e, white contours) suggests a
274 circulation driven by precipitating shallow convection^{37,39}. The alternative, sea-breeze
275 mechanism reaches lower levels³⁷. Both circulation types may exist over the Galapagos
276 (Extended Data Figure 8g): here, model meridional winds between 600-700hPa (shallow-
277 convection-type) are uncorrelated with those between 700-850hPa (sea-breeze-type),
278 indicating different physical processes at these two levels. The column dry static energy
279 budget (Methods) also implicates precipitating shallow convection. Model differences in this
280 budget are predominantly a balance between vertical advection integrated over 600-1000 hPa,
281 and precipitation latent heating (Extended Data Table 1, final column): in descending air
282 below 600 hPa, high- k_{qsat} models have stronger shallow advective warming from stronger
283 shallow descent, balancing weaker warming from weaker precipitation. As expected, the
284 ensemble mean in descending air is mostly a balance between radiative cooling and advective
285 warming.

286

287 Causality is hard to fully establish, but the most likely explanation of our results is that model
288 differences in k_{qsat} mostly originate from model differences in the behaviour of shallow
289 precipitating convection. Such differences would affect the sensitivity of precipitation to
290 SST directly. The consequent differences in shallow latent heating also appear to lead to
291 differences in shallow circulations. This couples shallow vertical velocities in descending
292 and ascending air (Extended Data Figure 8e), further modifying the sensitivity of
293 precipitation to SST.

294

295 Significant model differences in the physical representation of convection^{40,41}, including its
296 coupling to circulation^{5,42}, are well established. Improvements in k_{qsat} in the CNRM model

297 from CMIP5 (0.43 kg/g) to CMIP6 (0.54 kg/g) are largely associated with convection scheme
298 changes. Running CNRM-CM6 with the CNRM-CM5 convection scheme gives $k_{\text{qsat}}=0.36$
299 kg/g, even smaller than that of CNRM-CM5. That is, the effect of changing the convection
300 scheme is partly offset by changes in other schemes. Changes from CM5 to CM6 include the
301 shallow convection scheme and the transition from shallow to deep convection⁴³. These, and
302 other physics schemes, including boundary layer, deep or mid-level convection, or
303 microphysics, could all affect how shallow precipitating convection responds to SST.

304

305 Other processes may have smaller contributions. Dry shallow circulations⁴⁴ are more
306 important over hot, dry land. A limited role for differences in radiation (Extended Data Table
307 1, final column), suggests cloud parameterizations are not dominant. Differences in
308 dynamical schemes are thought to be less likely to be important for tropical precipitation
309 biases, although coupling of dynamics to physics is important⁴⁵⁻⁴⁷.

310

311 Models with stronger shallow circulations can also import more moist static energy in
312 ascending air, driving enhanced deep convection⁴⁸. Our results support this (Extended Data
313 Figure 8h), showing that model differences in shallow ascent are strongly positively
314 correlated with differences in deep ascent. This is an indirect link to k_{qsat} , which is more
315 weakly associated with deep ascent rates (Figure 5d).

316

317 **Strong real-world shallow circulations**

318 Shallow circulations are challenging to observe¹¹, but our results suggest they are stronger in
319 the real world than in most models. Models with high k_{qsat} (as in the real world) tend to have

320 strong shallow circulations (in both climate means and internal variability). We test this
321 further with two independent observations, in Aug-Oct. In models, there is a strong ($r=0.86$)
322 relationship between shallow descent, and northward trade winds (Figure 4c). If the shallow
323 descent is strong in the real world, we would expect strong northward trades – and this is
324 confirmed by QuikSCAT satellite observations⁴⁹ (SeaWinds scatterometer, Level 3 product,
325 years 1999-2009 - horizontal line in Figure 4c). There is, similarly, a strong ($r=0.81$)
326 relationship (Figure 4d) between 500-700hPa meridional winds over our study region, and
327 the mean 600-700hPa meridional wind over Galapagos and Christmas Islands (915 MHz
328 wind profiler^{8,50} observation sites, years 1994-2005 at Galapagos, 1990-2002 at Christmas
329 Island; few observations reach above 600hPa). If the large-scale 500-700hPa wind is strong
330 in the real world, we would expect strong southward winds in the observations, and this is
331 what the wind profilers show (horizontal line in Figure 4d). These results, using multiple
332 observations, confirm a previous suggestion based on a single reanalysis product⁵.

333

334 **Conclusions**

335 Our results show that k_{qsat} is linked to a range of model biases in precipitation and
336 atmospheric circulation. Improving k_{qsat} should reduce those biases, giving greater
337 confidence in seasonal through multi-decadal model projections. k_{qsat} affects the strength of
338 precipitation variation in both time and space. Other biases, in large-scale energy budgets,
339 and teleconnections, also affect precipitation. We show that k_{qsat} can be constrained by
340 observations, and give evidence that improving the representation of shallow tropical
341 precipitating convection, and its coupling to SST and circulation, could improve k_{qsat} . This
342 identifies specific model development goals and gives new ways of linking these to
343 observable physical processes.

345 **References**

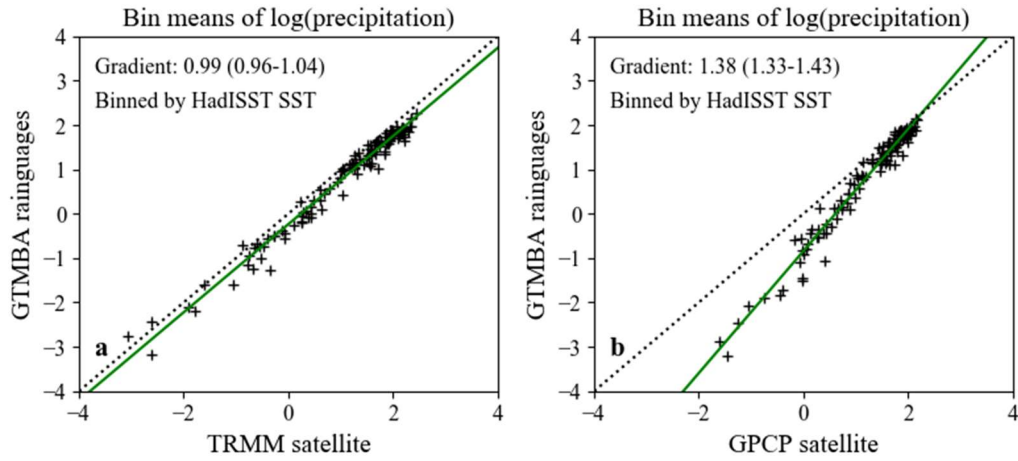
- 346 1. Philander, S. G. H. El-Nino Southern Oscillation Phenomena. *Nature* **302**, 295–301 (1983).
- 347 2. Pierrehumbert, R. T. Thermostats, Radiator Fins, and the Local Runaway Greenhouse. *J.*
348 *Atmos. Sci.* **52**, 1784–1806 (1995).
- 349 3. Tian, B. J. Spread of model climate sensitivity linked to double-Intertropical Convergence
350 Zone bias. *Geophys. Res. Lett.* **42**, 4133–4141 (2015).
- 351 4. Back, L. E. & Bretherton, C. S. Geographic variability in the export of moist static energy and
352 vertical motion profiles in the tropical Pacific. *Geophys. Res. Lett.* **33**, (2006).
- 353 5. Sherwood, S. C., Bony, S. & Dufresne, J. L. Spread in model climate sensitivity traced to
354 atmospheric convective mixing. *Nature* **505**, 37-+ (2014).
- 355 6. Trenberth, K. E., Stepaniak, D. P. & Caron, J. M. The global monsoon as seen through the
356 divergent atmospheric circulation. *J. Clim.* **13**, 3969–3993 (2000).
- 357 7. Back, L. E. & Bretherton, C. S. A Simple Model of Climatological Rainfall and Vertical Motion
358 Patterns over the Tropical Oceans. *J. Clim.* **22**, 6477–6497 (2009).
- 359 8. Zhang, C. D., Nolan, D. S., Thorncroft, C. D. & Nguyen, H. Shallow meridional circulations in
360 the tropical atmosphere. *J. Clim.* **21**, 3453–3470 (2008).
- 361 9. Li, R. & Fu, Y. F. Tropical precipitation estimated by GPCP and TRMM PR observations. *Adv.*
362 *Atmos. Sci.* **22**, 852–864 (2005).
- 363 10. Prakash, S., Mahesh, C. & Gairola, R. M. Comparison of TRMM Multi-satellite Precipitation
364 Analysis (TMPA)-3B43 version 6 and 7 products with rain gauge data from ocean buoys.
365 *Remote Sens. Lett.* **4**, 677–685 (2013).
- 366 11. Bellon, G., Reitebuch, O. & Naumann, A. K. Shallow Circulations: Relevance and Strategies for
367 Satellite Observation. *Surv. Geophys.* **38**, 1509–1528 (2017).
- 368 12. Li, G. & Xie, S. P. Tropical Biases in CMIP5 Multimodel Ensemble: The Excessive Equatorial
369 Pacific Cold Tongue and Double ITCZ Problems. *J. Clim.* **27**, 1765–1780 (2014).
- 370 13. Xie, S. P. *et al.* Towards predictive understanding of regional climate change. *Nat. Clim.*
371 *Chang.* **5**, 921–930 (2015).
- 372 14. Byrne, M. P. & Schneider, T. Energetic Constraints on the Width of the Intertropical
373 Convergence Zone. *J. Clim.* **29**, 4709–4721 (2016).
- 374 15. Bellenger, H., Guilyardi, E., Leloup, J., Lengaigne, M. & Vialard, J. ENSO representation in
375 climate models: from CMIP3 to CMIP5. *Clim. Dyn.* **42**, 1999–2018 (2014).
- 376 16. Zhang, X. X., Liu, H. L. & Zhang, M. H. Double ITCZ in Coupled Ocean-Atmosphere Models:
377 From CMIP3 to CMIP5. *Geophys. Res. Lett.* **42**, 8651–8659 (2015).
- 378 17. Hirota, N. & Takayabu, Y. N. Reproducibility of precipitation distribution over the tropical
379 oceans in CMIP5 multi-climate models compared to CMIP3. *Clim. Dyn.* **41**, 2909–2920 (2013).
- 380 18. Dixit, V., Geoffroy, O. & Sherwood, S. C. Control of ITCZ Width by Low-Level Radiative Heating
381 From Upper-Level Clouds in Aquaplanet Simulations. *Geophys. Res. Lett.* **45**, 5788-5797.
382 <https://doi.org/10.1029/2018GL078292> (2018).

- 383 19. He, J. *et al.* Precipitation Sensitivity to Local Variations in Tropical Sea Surface Temperature. *J.*
384 *Clim.* **31**, 9225–9238 (2018).
- 385 20. Rushley, S. S., Kim, D., Bretherton, C. S. & Ahn, M. S. Reexamining the Nonlinear Moisture-
386 Precipitation Relationship Over the Tropical Oceans. *Geophys. Res. Lett.* **45**, 1133–1140
387 (2018).
- 388 21. Bretherton, C. S., Peters, M. E. & Back, L. E. Relationships between water vapor path and
389 precipitation over the tropical oceans. *J. Clim.* **17**, 1517–1528 (2004).
- 390 22. Kanemaru, K. & Masunaga, H. A Satellite Study of the Relationship between Sea Surface
391 Temperature and Column Water Vapor over Tropical and Subtropical Oceans. *J. Clim.* **26**,
392 4204–4218 (2013).
- 393 23. TRMM. Tropical Rainfall Measuring Mission, TRMM (TMPA/3B43) Rainfall Estimate L3 1
394 month 0.25 degree x 0.25 degree V7, Greenbelt, MD, Goddard Earth Sciences Data and
395 Information Services Center (GES DISC), Accessed 2017. 10.5067/TRMM/TMPA/MONTH/7
396 (2011).
- 397 24. Huffman, G. J. *et al.* The TRMM multisatellite precipitation analysis (TMPA): Quasi-global,
398 multiyear, combined-sensor precipitation estimates at fine scales. *J. Hydrometeorol.* **8**, 38–55
399 (2007).
- 400 25. Adler, R. F. *et al.* The Global Precipitation Climatology Project (GPCP) Monthly Analysis (New
401 Version 2.3) and a Review of 2017 Global Precipitation. *Atmosphere (Basel)*. **9**, (2018).
- 402 26. McPhaden, M. J. *et al.* The tropical ocean global atmosphere observing system: A decade of
403 progress. *J. Geophys. Res.* **103**, 14169–14240 (1998).
- 404 27. McPhaden, M. J. *et al.* RAMA The Research Moored Array for African-Asian-Australian
405 Monsoon Analysis and Prediction. *Bull. Am. Meteorol. Soc.* **90**, 459–+ (2009).
- 406 28. Bourles, B. *et al.* The PIRATA program: History, accomplishments, and future directions. *Bull.*
407 *Am. Meteorol. Soc.* **89**, 1111–+ (2008).
- 408 29. Serra, Y. L., A’Hearn, P., Freitag, H. P. & McPhaden, M. J. ATLAS self-siphoning rain gauge
409 error estimates. *J. Atmos. Ocean. Technol.* **18**, 1989–2002 (2001).
- 410 30. Taylor, K. E., Williamson, D. & Zwiers, F. W. The sea surface temperature and sea-ice
411 concentration boundary conditions for AMIP II simulations. *PCMDI Rep. No. 60, Progr. Clim.*
412 *Model Diagnosis Intercomparison, Lawrence Livermore Natl. Lab. Livermore, California, 25 pp*
413 (2000).
- 414 31. Allen, M. R. & Ingram, W. J. Constraints on future changes in climate and the hydrologic cycle.
415 *Nature* **419**, 224–+ (2002).
- 416 32. Rayner, N. A. *et al.* Global analyses of sea surface temperature, sea ice, and night marine air
417 temperature since the late nineteenth century. *J. Geophys. Res.* **108**, (2003).
- 418 33. Huang, B. Y. *et al.* Extended Reconstructed Sea Surface Temperature Version 4 (ERSST.v4).
419 Part I: Upgrades and Intercomparisons. *J. Clim.* **28**, 911–930 (2015).
- 420 34. Hirahara, S., Ishii, M. & Fukuda, Y. Centennial-Scale Sea Surface Temperature Analysis and Its
421 Uncertainty. *J. Clim.* **27**, 57–75 (2014).
- 422 35. Biasutti, M., Sobel, A. H. & Kushnir, Y. AGCM precipitation biases in the tropical Atlantic. *J.*

- 423 *Clim.* **19**, 935–958 (2006).
- 424 36. Holloway, C. E. & Neelin, J. D. The convective cold top and quasi equilibrium. *J. Atmos. Sci.*
425 (2007) doi:10.1175/JAS3907.1.
- 426 37. Nolan, D. S., Powell, S. W., Zhang, C. D. & Mapes, B. E. Idealized Simulations of the
427 Intertropical Convergence Zone and Its Multilevel Flows. *J. Atmos. Sci.* **67**, 4028–4053 (2010).
- 428 38. Knutson, T. R. & Manabe, S. Time-mean response over the tropical Pacific to increased CO₂ in
429 a coupled ocean-atmosphere model. *J. Clim.* (1995) doi:10.1175/1520-
430 0442(1995)008<2181:TMROTT>2.0.CO;2.
- 431 39. Wu, Z. H. A shallow CISK, deep equilibrium mechanism for the interaction between large-
432 scale convection and large-scale circulations in the tropics. *J. Atmos. Sci.* **60**, 377–392 (2003).
- 433 40. Lin, Y. *et al.* TWP-ICE global atmospheric model intercomparison: Convection responsiveness
434 and resolution impact. *J. Geophys. Res. Atmos.* (2012) doi:10.1029/2011JD017018.
- 435 41. Randall, D. A. Beyond deadlock. *Geophys. Res. Lett.* (2013) doi:10.1002/2013GL057998.
- 436 42. Bony, S. & Dufresne, J. L. Marine boundary layer clouds at the heart of tropical cloud
437 feedback uncertainties in climate models. *Geophys. Res. Lett.* (2005)
438 doi:10.1029/2005GL023851.
- 439 43. Voltaire, A. *et al.* Evaluation of CMIP6 DECK Experiments With CNRM-CM6-1. *J. Adv. Model.*
440 *Earth Syst.* (2019) doi:10.1029/2019MS001683.
- 441 44. Nie, J., Boos, W. R. & Kuang, Z. Observational evaluation of a convective quasi-equilibrium
442 view of monsoons. *J. Clim.* (2010) doi:10.1175/2010JCLI3505.1.
- 443 45. Stevens, B. & Bony, S. What are climate models missing? *Science* (2013)
444 doi:10.1126/science.1237554.
- 445 46. Oueslati, B. & Bellon, G. Convective Entrainment and Large-Scale Organization of Tropical
446 Precipitation: Sensitivity of the CNRM-CM5 Hierarchy of Models. *J. Clim.* **26**, 2931–2946
447 (2013).
- 448 47. Vial, J., Bony, S., Stevens, B. & Vogel, R. Mechanisms and Model Diversity of Trade-Wind
449 Shallow Cumulus Cloud Feedbacks: A Review. *Surveys in Geophysics* (2017)
450 doi:10.1007/s10712-017-9418-2.
- 451 48. Fläschner, D., Mauritsen, T., Stevens, B. & Bony, S. The signature of shallow circulations, not
452 cloud radiative effects, in the spatial distribution of tropical precipitation. *J. Clim.* (2018)
453 doi:10.1175/JCLI-D-18-0230.1.
- 454 49. NASA. *SeaWinds on QuikSCAT Level 3 Surface Northward Wind for Climate Model Co*
455 *mparison. Ver. 1. PO.DAAC, CA, USA. Dataset accessed [2019-09-06] at*
456 *https://doi.org/10.5067/QS SNW-CMIP1.* (2012).
- 457 50. Gage, K. S., Williams, C. R. & Ecklund, W. L. UHF wind profilers: a new tool for diagnosing
458 tropical convective cloud systems. *Bull. - Am. Meteorol. Soc.* (1994) doi:10.1175/1520-
459 0477(1994)075<2289:UWPANT>2.0.CO;2.

461 **Figures**

462



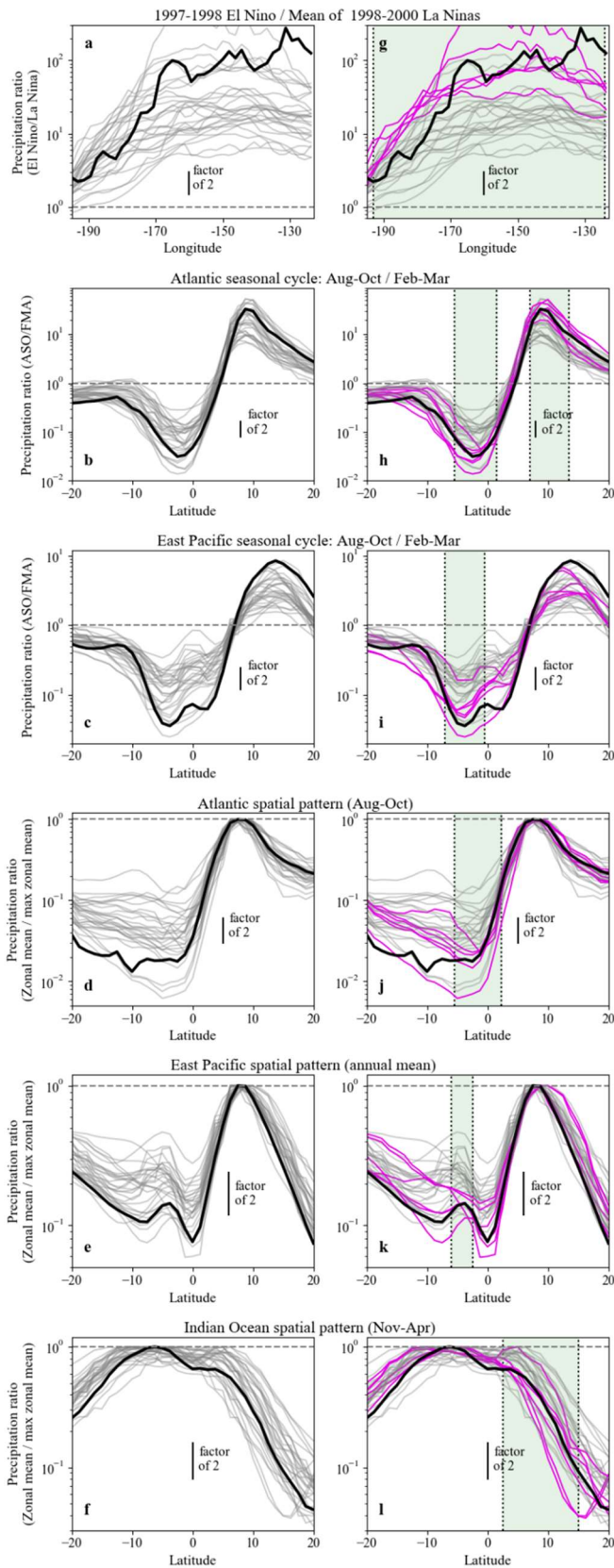
463

Figure 1.

464 Validating observations of log precipitation from satellites. GTMBA in-situ rain gauge
465 observations versus satellite observations from **a** TRMM and **b** GPCP. Each symbol
466 represents the mean of all seasonal mean data within a given SST bin (Methods). Green line:
467 best fit line (gradient and its 95% confidence interval quoted in each figure); dotted line: 1:1
468 line.

469

470



471

472 Figure 2. Model precipitation biases. (black) TRMM observations. Horizontal dashed line

473 marks precipitation ratio=1. **a-f** all CMIP5 models are shown in grey lines; **g-i** magenta:

474 'high- k_{qsat} ' subset; grey: other models. Spatial patterns (bottom 3 rows) given by scaling
475 zonal mean precipitation by its latitudinal maximum. Green shading marks the intervals used
476 for the 7 estimates of k_{qsat} . These examples were chosen as they feature large
477 differences/gradients in SST. Precipitation ratios are plotted because of the form of Equation
478 1.

479

480

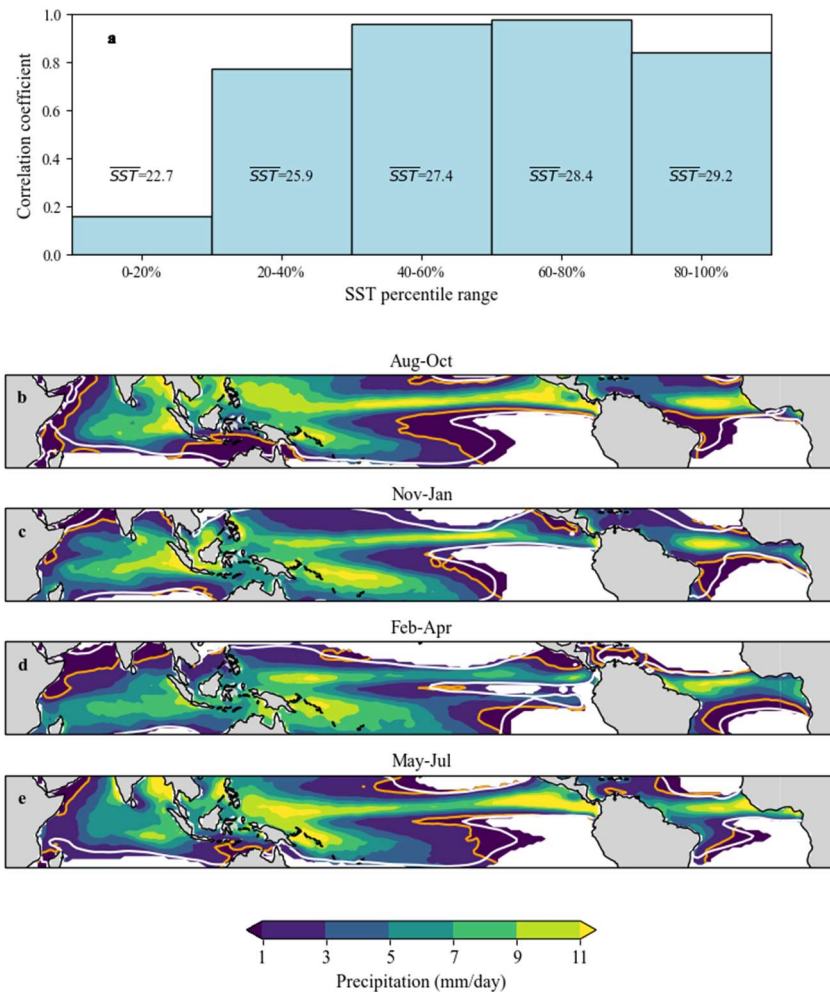


Figure 3. The region of

481

482

483

484

485

486

487

488

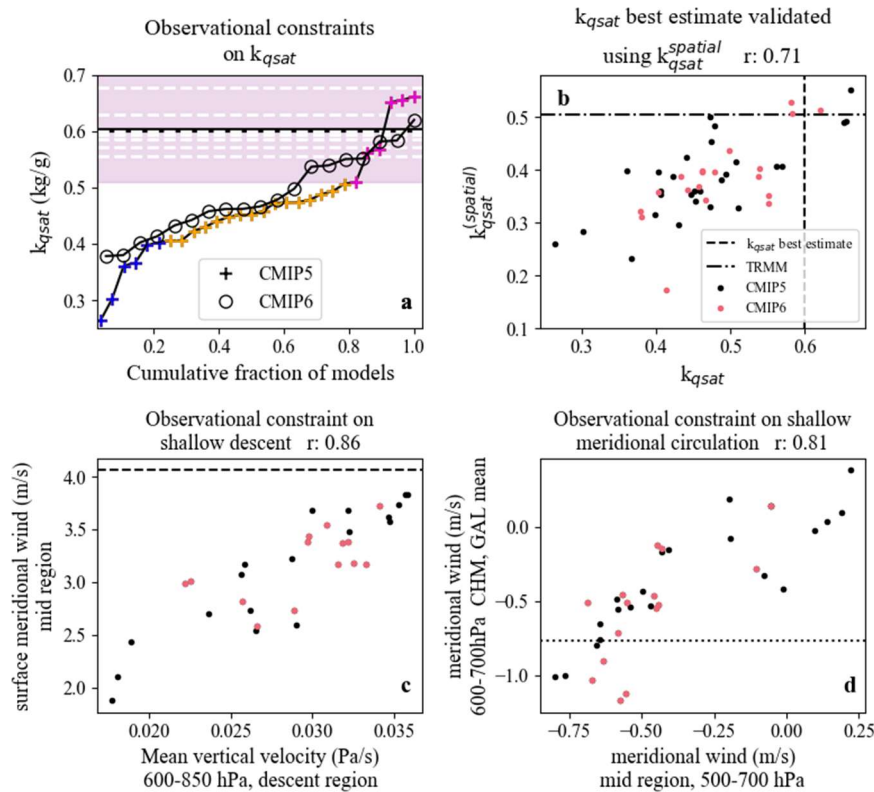
489

490

491

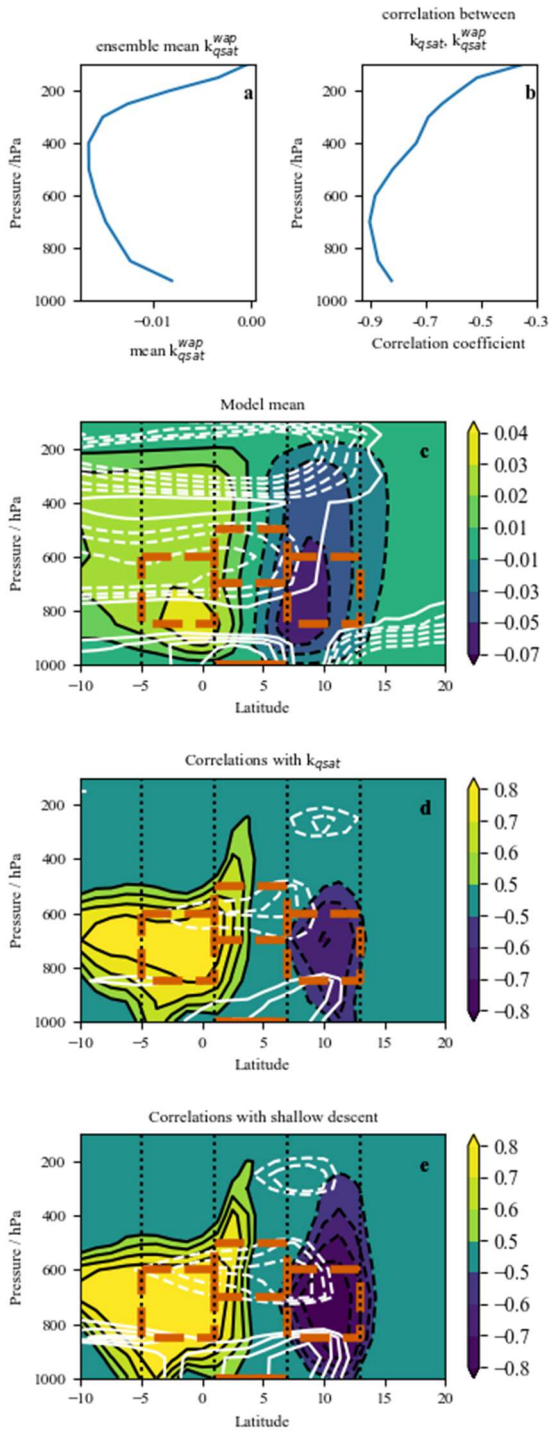
492

applicability of kqsat. (a) each bar represents a climatological zone covering 20% of the tropical oceans, defined by the seasonal climatological SSTs (e.g. the left bar is the zone with the coolest 20% of SSTs – white masked ocean in the maps below). Climatological zones are defined separately for each season. Bar height: the correlation coefficient, across CMIP5 models, between the standard calculation of kqsat, and that calculated only over the selected climatological zone. Mean SST (°C) for each zone is also shown. (b-e) Colours: mean TRMM precipitation; orange line highlights 1 mm/day contour. Data is masked over the 20% of the oceans where kqsat is inapplicable (left-hand bar in panel a shows low correlation). White contour shows the 30th percentile of SST: the standard calculation of kqsat uses data inside this contour.



493

494 Figure 4. High sensitivity of precipitation to SST, and strong shallow circulations, in the real
 495 world. **a** horizontal lines mark (white dashes) the 7 estimates of k_{qsat} (Extended data Figure
 496 6), and the central estimate (black solid); shading marks k_{qsat} values above our lower-bound
 497 estimate; symbols mark sorted model k_{qsat} values for (crosses) CMIP5 (blue and magenta
 498 denote low- k_{qsat} and high- k_{qsat} model subsets) and (circles) CMIP6. **b** $k_{qsat}^{(spatial)}$ versus k_{qsat} ,
 499 for each (black) CMIP5 and (red) CMIP6 model; horizontal line: $k_{qsat}^{(spatial)}$ from TRMM
 500 observations; vertical line: best estimate of k_{qsat} . **c,d** each symbol represents one CMIP5
 501 (black) or CMIP6 (red) model; title gives Pearson correlation coefficient. **c** surface
 502 meridional wind averaged over the mid-region (180W-10E, 1-7N) versus shallow descent
 503 index (defined in Figure 5); horizontal line marks QuikSCAT observation. **d** meridional wind
 504 averaged over Galapagos & Christmas island, 600-700hPa (few observations above 600hPa)
 505 versus meridional wind averaged over the mid region (180W-10E, 1-7N), 500-700hPa;
 506 horizontal line marks wind profiler observation.



507

508 Figure 5. Linking k_{qsat} to shallow circulations. **a,b** quantifies internal variability, and **c-e**
 509 climate means. **a** CMIP5 ensemble mean of k_{qsat}^{wap} (Pa kg/g), at each pressure level. **b** inter-
 510 model correlations (Pearson r) between k_{qsat} , and k_{qsat}^{wap} , at each pressure level. Correlations
 511 are negative because of the definition of wap . **c-e** Aug-Oct, 180W-10E zonal means. **c**
 512 CMIP5 ensemble mean of (colours) vertical velocity (Pa/s) and (white contours) meridional

513 wind. **d** inter-model correlations between k_{qsat} and mean vertical velocity (colours) and
514 between k_{qsat} and mean meridional wind (white contours). **e** as **d**, but for correlations with
515 the shallow descent index instead of k_{qsat} (shallow descent index = vertical velocity averaged
516 over left-hand orange-dashed box: 5S-1N, 850-600 hPa).

517

518

519
520

521 **Methods**

522

523 **Data domain, SST, precipitation and q_{sat}**

524 Results are based on seasonal means of precipitation and SST, over the tropical oceans (20S-
525 20N). q_{sat} is calculated as the saturation specific humidity at the seasonal mean sea-surface
526 temperature and 1000 hPa air pressure. Use of seasonal mean SST here means that q_{sat} will
527 be lower than the seasonal mean of saturation specific humidity calculated from daily SST
528 (due to sub-seasonal SST variability, and nonlinearity in the humidity calculation). We use
529 seasonal mean SST to minimise observational error: sub-seasonal SST variability is hard to
530 observe accurately.

531 **Observations**

532 Satellite precipitation data are seasonal averages of monthly means from V7 of the 3B43
533 Tropical Rainfall Measuring Mission (TRMM)^{23,24} dataset, covering 1998-2015. Data from
534 V2.3 of the Global Precipitation Climatology Project (GPCP²⁵) retrieval are included in
535 Figure 1 only.

536 In-situ raingauge data from 89 buoys of the Global Tropical Moored Buoy Array (all buoys
537 with more than 1 year of precipitation data), from the Tropical Ocean-Global Atmosphere
538 (TOGA²⁶) observing system, the Prediction and Research Moored Array in the Atlantic
539 (PIRATA²⁸) and the Research Moored Array for African-Asian-Australian Monsoon
540 Analysis and Prediction (RAMA²⁷), were retrieved as daily means. Days with lower quality
541 data (quality codes not equal to 1 or 2) were rejected. Monthly means were then calculated
542 only for months with 20 or more days with code 1 or 2 data (other months are marked as

543 missing). Seasonal means were taken only where three consecutive months had non-missing
544 data.

545 Monthly mean SSTs are taken from four different datasets. The CMIP5 AMIP dataset³⁰ (the
546 dataset used to drive the AMIP SST-forced model runs) is available only for 1980-2005.

547 This was used to calculate k_{qsat} for each model. For our observational estimate of a lower
548 bound on k_{qsat} (using TRMM precipitation), three SST datasets were used: HadISST³² version
549 1.1, ERSST³³ version 4 and COBE³⁴ version 2 (the AMIP dataset used by the model
550 simulations was not used, due to its limited temporal overlap with the TRMM operational
551 period).

552 Surface meridional wind observations are from SeaWinds on QuikSCAT Level 3, for the
553 period Aug 1999-Oct 2009. Wind profiler observations at San Cristóbal, Galápagos (0.9°S,
554 89.7°W, 1994-2005) and Christmas Island (2.8°N, 157.5°W, 1990-2002) used 915 MHz in
555 low mode, as used in other studies of shallow circulation⁸.

556 **Model data**

557 All model results are from atmosphere-only AMIP runs (one run per model version) forced
558 by observed SST, corresponding to the period 1980-2005. This includes 28 models from
559 CMIP5 (ACCESS1-0, ACCESS1-3, BNU-ESM, CCSM4, CESM1-CAM5, CNRM-CM5,
560 CSIRO-Mk3-6-0, CanAM4, GISS-E2-R, HadGEM2-A, IPSL-CM5A-LR, IPSL-CM5B-LR,
561 MIROC-ESM, MIROC5, MRI-AGCM3-2H, MRI-AGCM3-2S, MRI-CGCM3, NorESM1-M,
562 inmcm4, bcc-csm1-1-m, bcc-csm1-1, EC-EARTH, MPI-ESM-LR, MPI-ESM-MR,
563 FGOALS-s2, FGOALS-g2, GFDL-CM3, GFDL-HIRAM-C180) and 19 from CMIP6 (BCC-
564 CSM2-MR, BCC-ESM1, CAMS-CSM1-0, CanESM5, CNRM-CM6-1, CNRM-ESM2-1,
565 EC-Earth3-Veg, INM-CM4-8, INM-CM5-0, IPSL-CM6A-LR, MIROC6, HadGEM3-GC31-

566 LL, UKESM1-0-LL, MRI-ESM2-0, GISS-E2-1-G, GFDL-AM4, GFDL-CM4, NESM3,
567 SAM0-UNICON).

568 **Evaluation of satellite precipitation using GTMBA raingauge data**

569 First, seasonal mean satellite precipitation data (for all seasons) were interpolated linearly to
570 the GTMBA locations. Logarithms of seasonal mean precipitation were then taken, and all
571 datasets masked at times and locations where any data (GTMBA or satellite) were missing.
572 This resulted in 1723 observations of seasonal mean precipitation from each dataset, covering
573 the period 1998-2015 (the overlap between TRMM and GTMBA operational periods). For
574 the remainder of the analysis, the observation location and time are ignored.

575 To reduce noise effectively, while retaining the signal of interest, we use the fact that
576 precipitation tends to increase with SST, but the noise (as defined here) is largely
577 independent of SST. For each dataset, the 1723 observations were grouped into 120 bins (14
578 observations per bin). This was done by ranking the observations by seasonal mean SST (the
579 14 observations corresponding to the 14 lowest SST values were placed in the first bin, and
580 so on). The mean across each bin was then taken, giving 120 bin means of log(seasonal
581 precipitation): giving 120 symbols in Figure 1. 120 bins were chosen, as a mean over 14
582 observations is sufficient to reduce noise significantly, while retaining a large number of
583 symbols in Figure 1 to assess the method visually. Doubling the number of bins has
584 negligible effect on the gradient in Figure 1. Results are insensitive to which SST dataset is
585 used to bin the data (compare Extended data Figure 4, bottom two rows, with Figure 1).

586 We demonstrate that regression dilution bias is likely to be small in Figure 1a (method
587 justification in Methods subsection ‘Estimating regression dilution bias’ below). We do this
588 by repeating the analysis in Figure 1a, but regressing first TRMM against GPCP (Extended

589 data Figure 4, top left), then GPCP against TRMM (Extended data Figure 4, top right). The
590 product of the two regression gradients is 0.98 (close to 1), suggesting that this bias is small.

591 We also tested sensitivity of the validation to potential undercatch by the GTMBA raingauges
592 in windy conditions²⁹. This issue could only bias the gradients in Figures 1a,b if the
593 percentage undercatch varied systematically from low to high precipitation (because Figure 1
594 shows log precipitation). To test this, we recalculated the gradients in Figures 1a,b, but after
595 masking the data according to the seasonal mean wind speed (also observed by GTMBA
596 buoys). Gradients calculated for low wind (0-4 m/s; 22% of all data) and high wind (6-10
597 m/s; 27% of all data) show no significant differences from Figure 1a,b (for TRMM,
598 confidence intervals consistently spanning 1 and best estimate within 5% of 1; for GPCP,
599 confidence intervals consistently excluding 1). This suggests that the satellite validation is
600 insensitive to wind undercatch.

601 **Figure 2 data preparation (regions, seasons, time periods)**

602 For Figure 2, all data is first regridded by area-averaging to a common grid (resolution: 1.25°
603 latitude by 1.875° longitude).

604 The El Niño/La Niña ratio is based on large ENSO episodes in years both simulated by the
605 models and observed by TRMM: the 1997-1998 El Niño divided by the mean of 1998-1999
606 and 1999-2000 La Niñas, for the El Niño peak season (November-January), averaged over
607 10S-10N.

608 Other data are zonal means over the following longitude bands (with land masked out):
609 (Atlantic) 70W-25E; (East Pacific) 150-100W; (Indian Ocean) 50-100E.

610 Seasonal cycles over Atlantic and Pacific are calculated as the zonal mean for August-
611 October divided by the zonal mean for February-April). These seasons were chosen because

612 they show large differences in SST, but small differences in solar zenith angle (the latter can
613 affect precipitation by altering land temperature).

614 Spatial patterns are calculated, for each model/observational dataset, as the zonal mean at
615 each latitude, divided by the maximum, zonal mean for the same model/observational dataset.
616 This was calculated for August-October (ASO) for the Atlantic, due to the large meridional
617 SST gradient for this season. November-April was used for the Indian Ocean, as this basin
618 has a significant meridional SST gradient for this period.

619 **Estimating k_{qsat} , part 1: data preparation**

620 k_{qsat} is used here specifically to rank the models and compare with observations. Therefore,
621 the method of calculation needs to be consistent across models and observations, and to
622 minimise the potential for observational error.

623 For each year, for a given season, the logarithm of seasonal mean precipitation is calculated.
624 The spatial pattern of climatological mean precipitation (Extended data Figure 2j) is
625 dominated by a small area of large precipitation (occupying around 10% of the area). Hence,
626 if we evaluated k_{qsat} without taking the logarithm, our result would be dominated by this
627 small area of the tropics. The spatial distribution of $\log(\text{precipitation})$ is much more uniform
628 (Extended data Figure 2k), except for the driest 10% of the tropics (which is eliminated from
629 our analysis as we mask the region of coolest SST). Hence, using $\log(\text{precipitation})$ to
630 calculate k_{qsat} ensures that the result is influenced fairly equally by all parts of our analysis
631 region (confirmed in Figure 3a). Our results use seasonal mean precipitation. Use of other
632 timescales would alter k_{qsat} , due to the (nonlinear) logarithm in Equation 1.

633 For models, k_{qsat} is calculated using data on each model's native grid. For observations, q_{sat}
634 is regridded linearly to the high resolution TRMM horizontal grid.

635 Before estimating k_{qsat} , to minimise observational error, we exclude the 30% of the tropical
636 oceans with the lowest climatological mean SST. An advantage of using a logarithm in
637 equation 1 is that k_{qsat} estimates are not dominated by the narrow ITCZ region. However, it
638 could mean that error in observing the very lowest rainfall rates could cause large error in our
639 real-world estimate of k_{qsat} . Therefore we mask the regions with coolest SST on average.
640 This masking is only done in calculating k_{qsat} . It is not done in Figure 2, as the climatological
641 means reduce observational error there.

642 At each location, anomalies relative to climatological means are calculated for each year, for
643 both q_{sat} and $\log(\text{precipitation})$. Locations that have missing data in any year are excluded.
644 These data are used in the sortav method, described below.

645 **Estimating k_{qsat} , part 2: sortav regression method**

646 Once the data is prepared as above, our regression method for estimating k_{qsat} (denoted
647 ‘sortav’) is applied. For python code for this method, and an illustrative example, see Code
648 Availability Statement. The sortav method is designed to prevent dominance from the SST
649 spatial pattern associated with ENSO (an issue because ENSO features large SST anomalies
650 in a consistent pattern). In estimating k_{qsat} from inter-annual variability, our aim is to reduce
651 the ‘other-processes’ term in Equation 1, by averaging over different SST patterns, with
652 different patterns of large-scale circulation anomalies. If a single SST pattern (ENSO) was
653 allowed to dominate, this would not be effective. If standard linear regression was used, the
654 ENSO pattern would dominate, because ENSO features large SST anomalies. In addition,
655 tropical means of precipitation and SST can vary over time, involving different processes
656 than those represented by k_{qsat} . Our method avoids these issues.

657 The first step sorts each year of data. Say the data has n locations and y years. For each year,
658 the n anomalies in $\log(\text{precipitation})$ are sorted in order of increasing q_{sat} anomaly. This

659 produces, for each year, a vector of length n , with the first element corresponding to the
660 location with the most negative q_{sat} anomaly, and the last element being that with the most
661 positive q_{sat} anomaly. If Equation 1 was exactly true, with zero noise, each vector would be
662 sorted in order of increasing anomaly in $\log(\text{precipitation})$. Because of the noise (from large-
663 scale processes), this is not, in general, true. This gives y sorted vectors, each of length n .

664 We then average over the y years, to produce one mean vector of length n (e.g. the 1st
665 element of this vector is the mean of the y precipitation anomalies found over the most
666 negative q_{sat} anomaly from each year). This averaging removes much of the noise, because
667 the noise is largely independent of q_{sat} . In this mean, years with large SST anomalies have
668 the same weighting as other years, avoiding dominance by ENSO.

669 The same process is repeated for q_{sat} . This gives two mean vectors, each of length n : for
670 anomalies in $\log(\text{precipitation})$ and in q_{sat} .

671 The relationship between the averaged anomalies in $\log(\text{precipitation})$ and q_{sat} is relatively
672 linear in both models and observations (e.g. Extended data Figure 2a-d), suggesting that
673 Equation 1 is a useful approximation in this context. $k_{q_{\text{sat}}}$ is then estimated from these vectors,
674 by ordinary least squares linear regression (e.g. the gradients of the best fit lines in Extended
675 data Figure 2a-d).

676 To compare with our sortav method, alternative estimates of $k_{q_{\text{sat}}}$ (marked OLS in Extended
677 Data Figures 2h,7) use standard linear regression between seasonal anomalies in
678 $\log(\text{precipitation})$ and q_{sat} (without sort-averaging).

679

680 **Calculating $k_{q_{\text{sat}}}^{\text{(spatial)}}$ and $k_{q_{\text{sat}}}^{\text{spattemp}}$**

681 $k_{qsat}^{(spatial)}$ is calculated using the same method as k_{qsat} , except that it quantifies seasonal and
682 spatial variation in time-mean climate (in contrast with k_{qsat} , which quantifies interannual
683 variability). First, time means are taken for each dataset and season (giving 4 season means
684 per grid point per dataset). For each dataset and each season separately, precipitation is
685 divided by the tropical mean, before taking logarithms. This is done to scale out model
686 variation in the tropical mean (which is controlled by the large-scale energy budget). For q_{sat} ,
687 for each dataset and season separately, anomalies are taken with respect to the tropical mean.
688 Masking, to exclude regions with low q_{sat} , is based on annual mean q_{sat} .

689 $k_{qsat}^{spattemp}$ is defined as follows:

$$690 \quad P/\bar{P} \approx \exp(k_{qsat}^{spattemp} \cdot q_{sat}')$$

691 This approximates variation in precipitation relative to the tropical mean, driven by variation
692 in q_{sat} relative to its tropical mean. The overbar represents the tropical mean for the current
693 season of the current year, and q_{sat}' is specifically the q_{sat} anomaly with respect to the
694 tropical mean:

$$695 \quad q_{sat}' = q_{sat} - \overline{q_{sat}}$$

696 Anomalies expressed this way capture temporal and spatial variability associated with
697 variation in local SSTs, but exclude temporal variability in tropical mean precipitation (which
698 is constrained by the large-scale atmospheric energy budget).

699 $k_{qsat}^{spattemp}$ is estimated using the same approach as k_{qsat} , but anomalies of $\log(P)$ and q_{sat}
700 are taken relative to their tropical means for the corresponding season and year (k_{qsat} is
701 evaluated using anomalies with respect to local climatological means for each location).

702 A disadvantage of both $k_{q_{sat}}^{(spatial)}$ and $k_{q_{sat}}^{spattemp}$ is that they have some sensitivity to other
703 processes (teleconnections) associated with the specific spatial patterns in climatological
704 mean SST (these spatial patterns are filtered out less effectively as there are only 4 seasons,
705 compared to the 25 years of internal variability used to estimate $k_{q_{sat}}$).

706

707 **A lower bound for $k_{q_{sat}}$, using observed interannual variability**

708 This method (estimated lower bound on $k_{q_{sat}}$) accounts for three forms of observational error,
709 combined using Monte Carlo sampling.

710 First, systematic error in the observed magnitudes of seasonal mean SST anomalies could
711 bias $k_{q_{sat}}$. To explore this, we first estimated $k_{q_{sat}}$ (with the sortav method) using TRMM
712 precipitation, and each of the three SST datasets (HadISST, ERSST, COBE) that cover the
713 whole TRMM operational period, giving three direct, unscaled estimates of $k_{q_{sat}}$ (Extended
714 data Table 2a).

715 Second, error in the SST spatial pattern will cause a low bias in $k_{q_{sat}}$ (regression dilution
716 bias). Typical magnitudes of this bias are estimated (see more detail in Methods section
717 ‘Estimating regression dilution bias’). This is done by regressing pairs of SST datasets
718 against each other, with regression coefficients calculated using the sortav method (as used
719 for $k_{q_{sat}}$). Extended data Table 2b shows the results for each pair of SST datasets. The final
720 column of Extended data Table 2b gives the 6 different estimates of regression dilution bias.

721 Third, the TRMM operational period does not fully overlap the AMIP SST-forced model
722 simulation period. Thus, $k_{q_{sat}}$ estimated for the TRMM period will be different from that
723 obtained if TRMM were operational throughout the AMIP period (due to a different set of
724 SST patterns during the TRMM and AMIP period). Estimates of typical magnitudes of this

725 error were obtained using samples from coupled ocean-atmosphere simulations (Extended
726 data Figure 7), giving 85 samples of percentage error.

727 10000 estimates of k_{qsat} were then generated using Monte Carlo sampling. For each estimate,
728 one of the three direct estimates (Extended data Table 2a) was selected at random, ‘corrected’
729 by a random selection from the 85 samples of percentage error (Extended data Figure 7), and
730 further corrected using a random selection from the 6 estimates of regression dilution bias
731 (Extended data Table 2b).

732 The lower bound of the 95% confidence interval of these 10000 estimates is then taken. We
733 only use the lower bound for the following reason: it seems unlikely that the true regression
734 dilution bias is weaker than the minimum value estimated here (around 10%, Extended data
735 Table 2b). This is because we do not expect the SST datasets to be significantly closer to the
736 real SST than they are to each other. However, it is plausible that the regression dilution bias
737 could be larger than estimated, so we do not quote an upper bound for k_{qsat} .

738 The appropriate lower bound for an atmosphere-only AMIP model may be even higher than
739 our quoted result, as the observed k_{qsat} value may be reduced by the effect of atmospheric
740 internal variability on SST¹⁹. k_{qsat} values from AMIP models are similar to or higher than
741 from the equivalent coupled models. In contrast, this coupling issue should be small for our
742 central estimate of k_{qsat} (next section), as that is based on metrics where ocean dynamics (for
743 ENSO) or forcing associated with the mean state/seasonal cycle dominate the SST
744 differences/gradients.

745 **Central estimate of k_{qsat} in the real world**

746 We start by finding where, geographically, the models are most sensitive to k_{qsat} . This is
747 done using correlation coefficients (r) between k_{qsat} and the log of precipitation ratios

748 (Extended data Figure 5) for each latitude (or longitude for ENSO) in each panel in Figure
749 2. This reveals six discrete intervals (shaded in Figure 2) where $|r| > 0.6$ (about 50% variance
750 explained), and a seventh, showing weaker correlations, over the Indian Ocean. For each
751 model, we average the log of precipitation ratios over each interval, and take the difference
752 from the equivalent value for TRMM. This gives seven error indices for each model (y-axes
753 in Extended data Figure 6). For each interval, the 28 model error indices are regressed
754 against k_{qsat} (x-axes in Extended data Figure 6), and k_{qsat} is estimated from where the line of
755 best fit crosses zero error. This gives seven estimates of k_{qsat} ; their mean is our central
756 estimate.

757 We did not use the coupled ocean-atmosphere models to estimate k_{qsat} , due to the evident
758 residual biases from SST error in these models, and because it isn't possible to use the ENSO
759 response for coupled models, due to model differences in simulations of ENSO SST
760 responses.

761 **Estimating regression dilution bias**

762 Regression dilution bias⁵¹ arises when there is random error in the independent variable (e.g.
763 q_{sat} in estimating k_{qsat}). This causes the regression gradient to be biased low. This bias
764 reduces the gradient by a factor (β) that depends only on the characteristics of the
765 independent variable. We estimate typical magnitudes of this bias using different
766 observations of the independent variable (e.g. different SST datasets), as follows.

767 Say the vector of true values of the independent variable is \mathbf{x} , and we have two different
768 observational estimates, $\mathbf{x1}$ and $\mathbf{x2}$. We first regress $\mathbf{x1}$ against $\mathbf{x2}$. This regression uses the
769 same methodology as when regressing the dependent variable against \mathbf{x} : i.e. for estimating
770 dilution bias in observations of k_{qsat} , the sortav method is applied; and for the satellite
771 precipitation validation, the SST binning is used. The regression gradient (f_{12}) obtained from

772 regressing **x1** against **x2**, will be biased low by a factor β_2 (from error in **x2**). We then
773 regress **x2** against **x1**. This regression gradient (f_{21}) will be biased low by a factor β_1 (from
774 error in **x1**).

775 We then estimate the dilution bias as:

$$776 \quad \beta \approx \text{sqrt}(\beta_2 \cdot \beta_1) = \text{sqrt}(f_{12} \cdot f_{21})$$

777 (with no dilution bias, $f_{12} \cdot f_{21} = 1$, by definition).

778 This method assumes that the errors in **x1** and **x2** are independent.

779 **Column dry static energy budget (DSE)**

780 Dry static energy (DSE) is given by $s = c_p T + gz$, where c_p is the specific heat at constant
781 pressure, T is the temperature, g is the gravitational acceleration, and z is altitude). DSE is
782 affected by advection, precipitation, radiation and sensible heat:

$$783 \quad -\langle \omega \frac{\partial s}{\partial p} \rangle - \langle v \cdot \nabla s \rangle + LP + R + Q_{turb} = 0,$$

784 where ω is the vertical pressure velocity, p is pressure, v is horizontal wind. Angle brackets
785 represent the mass-weighted vertical integral from 1000-100hPa. The first term represents
786 import of DSE via column-integrated vertical advection; the second is horizontal advection.
787 P is the total surface precipitation and L the latent heat of condensation; R is net radiation
788 into the atmospheric column; and Q_{turb} is the surface sensible heat flux.

789

790 **Methods References**

791

792 51. Hutcheon, J. A., Chiolero, A. & Hanley, J. A. Random measurement error and regression
793 dilution bias. *Br. Med. J.* **340**, (2010).

794

795 **Data availability**

796 Datafiles with estimates of k_{qsat} for models and observations, along with sample plotting
797 code, are available from <http://doi.org/10.5281/zenodo.3878691>. Data from the integration of
798 CNRM-CM6 with the CM5 convection scheme (denoted CNRM-CM6-conv5) are available
799 from <https://doi.org/10.5281/zenodo.3875005>. Model and observational data is available at the
800 following websites. CMIP5: <https://cmip.llnl.gov/cmip5/>; CMIP6: [node.llnl.gov/projects/cmip6/](https://esgf-
801 node.llnl.gov/projects/cmip6/); GTMBA: <https://www.pmel.noaa.gov/gtmba/>; TRMM:
802 <https://pmm.nasa.gov/data-access/downloads/trmm>; GPCP and COBE:
803 <https://www.esrl.noaa.gov/psd/>; HadISST: <https://www.metoffice.gov.uk/hadobs/hadisst>; ERSST:
804 <http://www1.ncdc.noaa.gov/pub/data/cmb/ersst/v4/netcdf/> .

805 **Code Availability**

806 Python code for calculating k_{qsat} , including the sortav regression routine, is available from
807 <http://doi.org/10.5281/zenodo.3878691>.

808

809

810

811

812 **End Notes**

813

814 **Acknowledgements** This work was supported jointly by the Met Office Hadley Centre Climate
815 Programme funded by BEIS and Defra, and by the Newton Fund through the Met Office Climate
816 Science for Service Partnership Brazil (CSSP Brazil). SSR was supported by the National Aeronautics
817 and Space Administration Grant 80NSSC17K0227 and the Korean Meteorological Administration
818 Research and Development Program under grant KMI2018-03110. We acknowledge the GTMBA
819 Project Office of NOAA/PMEL for making the GTMBA data available. The QuikSCAT data were
820 obtained from the NASA EOSDIS Physical Oceanography Distributed Active Archive Center
821 (PO.DAAC) at the Jet Propulsion Laboratory, Pasadena, CA ([http://dx.doi.org/10.5067/GHGMR-](http://dx.doi.org/10.5067/GHGMR-4FJ01)
822 [4FJ01](http://dx.doi.org/10.5067/GHGMR-4FJ01)). We acknowledge NOAA/ESRL PSD for the wind profiler data. We acknowledge the World
823 Climate Research Programme's Working Group on Coupled Modelling, which is responsible for CMIP,
824 and we thank the climate modelling groups (listed in Methods) for producing and making available
825 their model output. For CMIP the U.S. Department of Energy's Program for Climate Model Diagnosis
826 and Intercomparison provides coordinating support and led development of software infrastructure
827 in partnership with the Global Organization for Earth System Science Portals. GPCP data provided by
828 the NOAA/OAR/ESRL PSD, Boulder, Colorado, USA, from their Web site at
829 <https://www.esrl.noaa.gov/psd/>. COBE-SST2 data provided by the NOAA/OAR/ESRL PSD, Boulder,
830 Colorado, USA, from their Web site at <https://www.esrl.noaa.gov/psd/>

831 **Author Contributions** P.G. conceived and designed the study and performed the analysis. All

832 authors contributed to scientific interpretation and wrote the manuscript. R.R. performed the

833 CNRM model simulations. P.G., R.C., C.E.H. and R.R. contributed understanding on physical
834 processes. J.K. provided knowledge of SST observational uncertainty and datasets.

835 **Author Information** Reprints and permissions information is available at www.nature.com/reprints.

836 The authors have no competing financial interests. Correspondence and requests for materials
837 should be addressed to peter.good@metoffice.gov.uk.

838

839

840

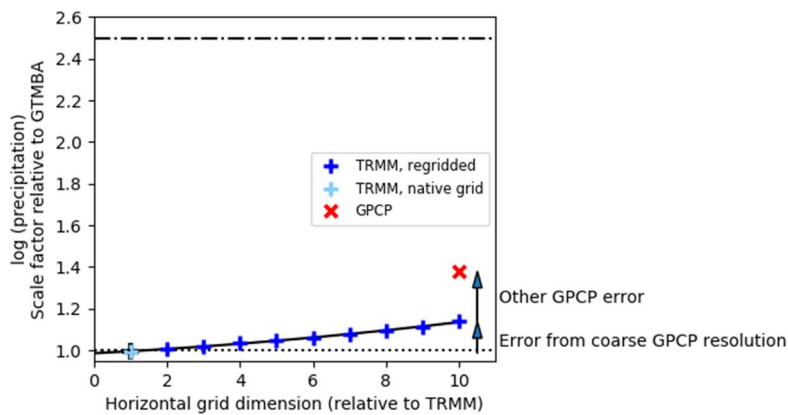
841

842

843

844 **Extended Data Figures**

845



846

847 Extended data Figure 1. Effect of low spatial resolution in GPCP satellite observations of

848 log(seasonal precipitation). y-axis: regression gradient in validation against GTMBA

849 raingauge data (i.e. gradients in Figure 1 for light blue and red symbols). x-axis: horizontal

850 grid dimension relative to TRMM (e.g. the TRMM resolution is 0.25° , ten times smaller than

851 the GPCP resolution of 2.5° , so the red symbol is placed at $x=10$). Dark blue symbols:

852 results when TRMM data is regridded (by area averaging) to coarser grids. The coarser grids

853 are chosen so the grid box edges overlap edges of the native TRMM grid. To give the errors

854 context, the dash-dot line marks the ratio between the largest and smallest model values of

855 k_{qsat} (2.5). Solid black line is a quadratic least-squares best fit line through the TRMM-based

856 data. The intercept of the TRMM best-fit curve at $x=0$ (i.e. infinitely fine grid) is very close

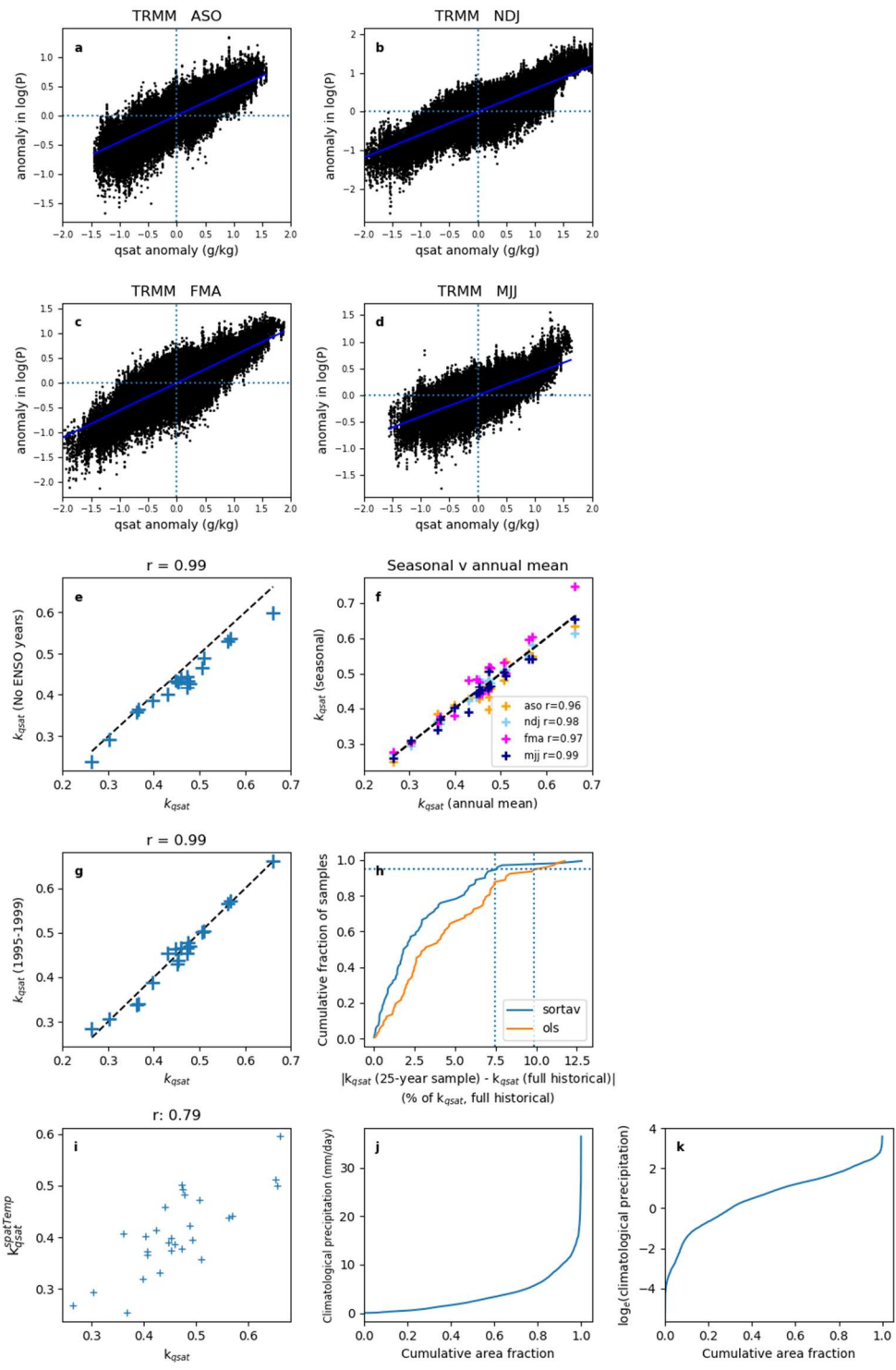
857 to the value estimated on the TRMM native grid (light blue symbol), indicating that the

858 TRMM grid is sufficiently fine for comparison with the raingauge data on seasonal

859 timescales.

860

861



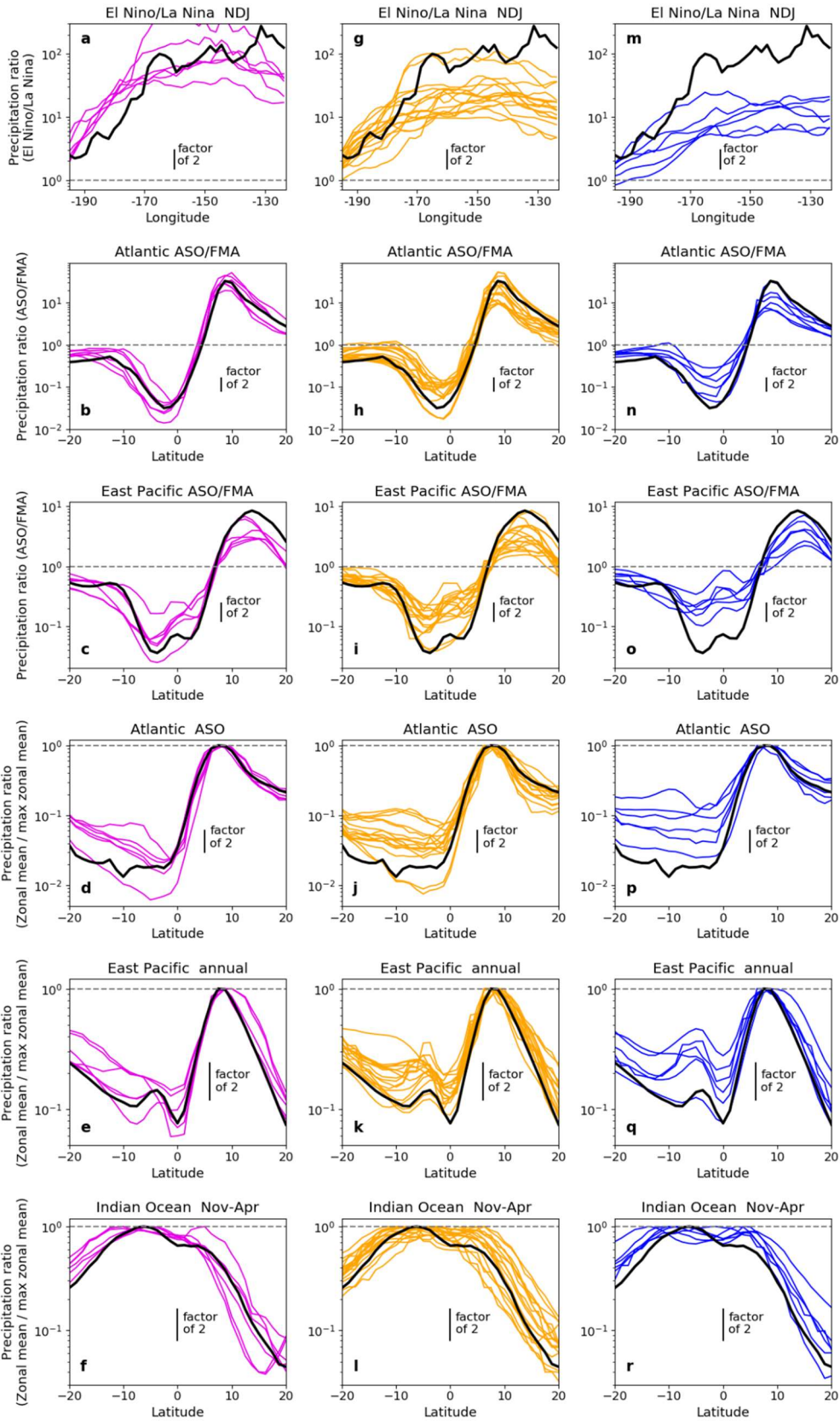
862

863 Extended data Figure 2. Testing the method of estimating k_{qsat} . **a-d**: example results of the
 864 sortav method for TRMM precipitation and HadISST SST, for different seasons: mean
 865 vectors of anomalies in (y-axis) $\log(\text{precipitation})$ and (x-axis) q_{sat} ; k_{qsat} is given by the
 866 gradient of the blue best-fit regression line. **e**, y-axis: k_{qsat} calculated after excluding the 9

867 years with the largest absolute value of the nino3.4 index; x-axis: default k_{qsat} (one symbol
868 per model); k_{qsat} is on average 6% lower when ENSO years excluded, due to a small
869 sensitivity to the ENSO characteristic spatial pattern; but the model ranking is largely
870 unchanged ($r = 0.99$). **f**, k_{qsat} calculated for individual seasons versus the annual mean value;
871 **g** k_{qsat} using only years 1995-1999 versus the full 25-year estimate; **h**, estimating variability
872 (due to internal variability in SST patterns) in k_{qsat} estimated from 25 years of data: for each
873 coupled ocean-atmosphere model, k_{qsat} is estimated both for the full historical run, and for all
874 25-year chunks. Panel shows the cumulative distribution function of absolute percentage
875 differences between the 25-year estimates and the full estimates (95% of samples are within
876 8% of the long-term value from the full historical run). This panel shows results for two
877 methods of estimating k_{qsat} : our 'sortav' method (as used throughout the manuscript), and
878 standard OLS regression between seasonal anomalies in $\log(\text{precipitation})$ and q_{sat} . **i**
879 comparing $k_{qsat}^{spattemp}$ with k_{qsat} ; each cross represents one CMIP5 model. **j,k** Cumulative
880 distribution functions of **j** climatological mean precipitation and **k** $\log(\text{precipitation})$. From
881 HadGEM2-A, May-July season (same picture seen in other seasons).

882

883



884

885 Extended data Figure 3. Model biases for the high, mid-range and low- k_{qsat} models
 886 separately. As Figure 2, for **a-f** high- k_{qsat} models; **g-l** mid- k_{qsat} models; **m-r** low- k_{qsat} models.

887

888 Extended data Figure 4. Testing potential errors in the satellite validation against GTMBA.

889 **a,b** testing for regression dilution bias from error in TRMM observations: as Figure 1, but for

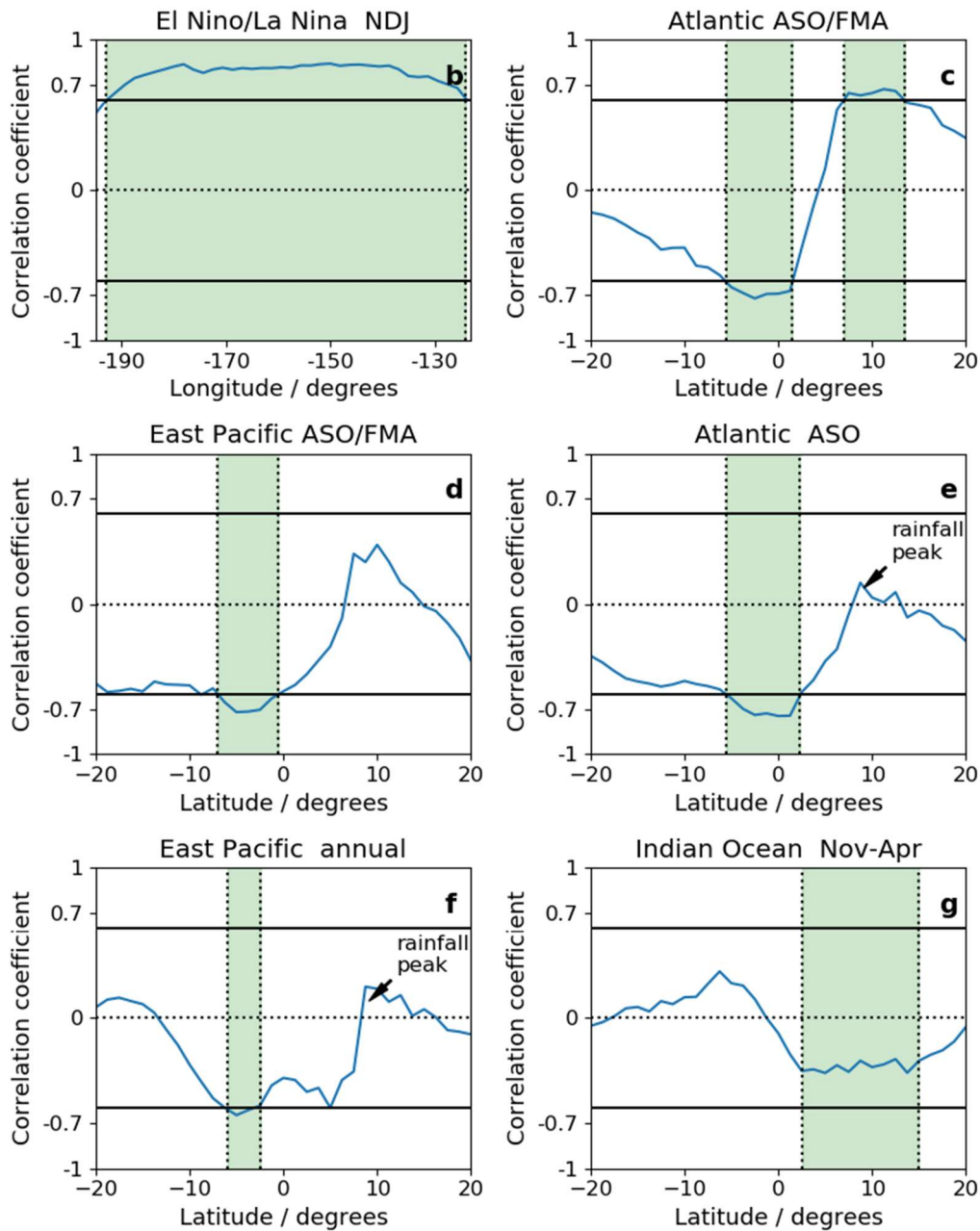
890 **a** TRMM versus GPCP (both interpolated to GTMBA sites and masked as in Figure 1) and **b**

891 GPCP versus TRMM. **c-f** testing for effects of SST uncertainty on the binning: as Figure 1,

892 but using **c,d** ERSST and **e,f** COBE SST datasets to bin the data.

893

894



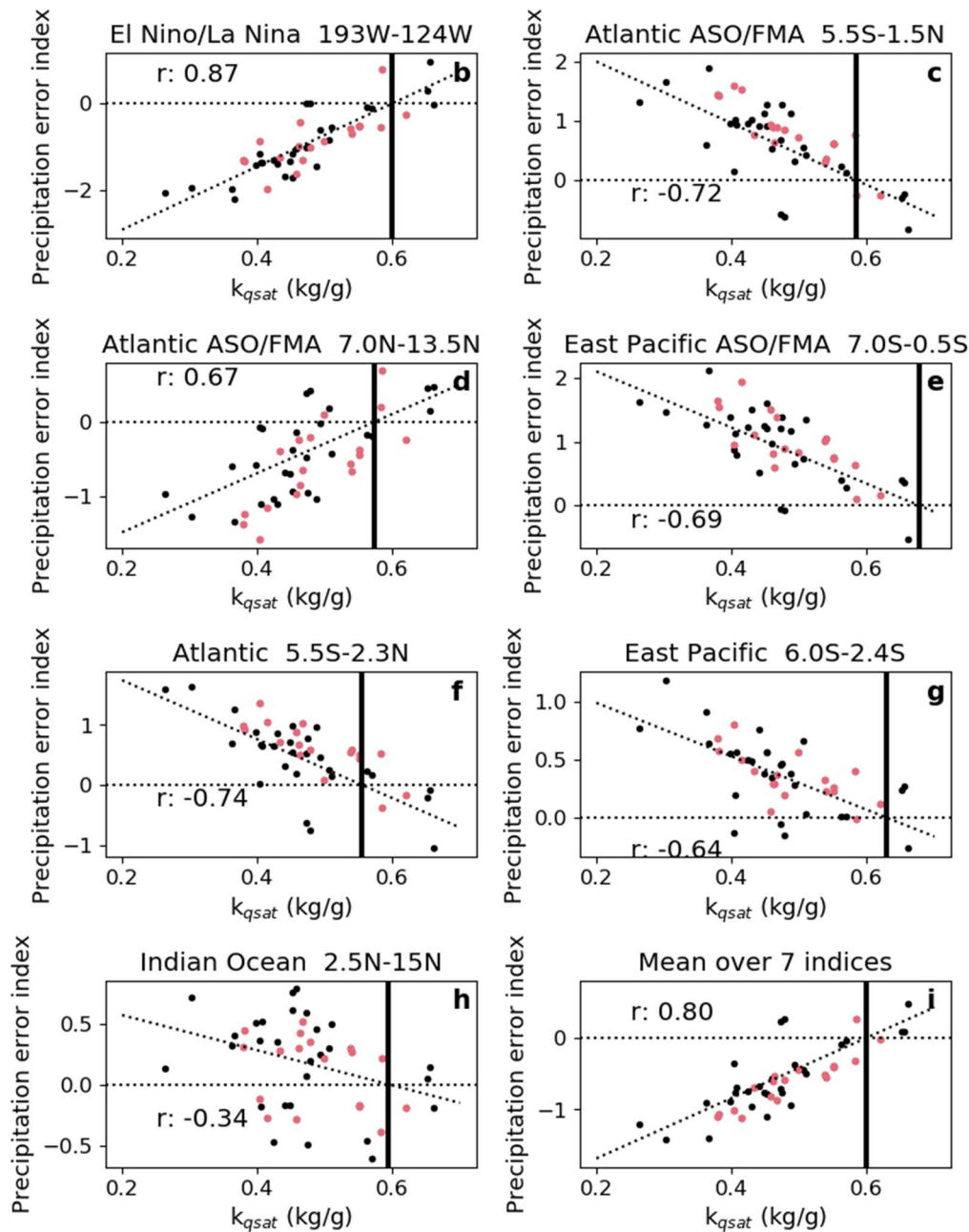
895

896 Extended data Figure 5. Regions where models are most sensitive to k_{qsat} . For each latitude
 897 of each region: y-axis shows Pearson correlation coefficients (r) between the 28 different
 898 CMIP5 model values k_{qsat} , and the 28 CMIP5 model values of the logarithm of the
 899 precipitation ratio for that latitude and region (i.e. the logarithm of the grey lines in Figure 2a-
 900 f). Green bands mark the latitude intervals chosen to estimate the observational constraints
 901 on k_{qsat} (**a-e**: intervals chosen where $|r| > 0.6$; **f**, a band of most negative r is chosen).
 902 Coefficients close to zero near 8N in the Atlantic and East Pacific spatial patterns correspond

903 to the latitude of the precipitation peak in most models (the model spread in the precipitation
904 peak is scaled out; coefficients are not exactly zero as there is a small model spread in the
905 latitude of the precipitation peak).

906

907



908

909 Extended data Figure 6. Scatter plots underpinning the central observational estimate of k_{qsat} .

910 **a-g** Precipitation error index versus k_{qsat} for each of the 7 latitude intervals highlighted in

911 Figure 2. Y-axes: logarithm of precipitation ratio, averaged over each latitude band, minus

912 the equivalent value for TRMM observations, for (black) CMIP5 and (red) CMIP6 models.

913 Dotted lines: linear least-squares fits (using CMIP5 data only). Vertical black line: k_{qsat}

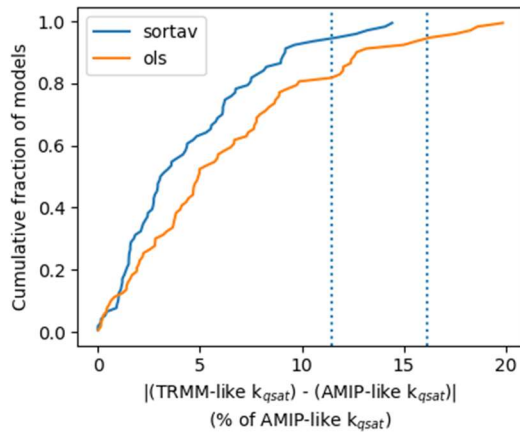
914 estimate for each latitude interval, from the intercept of the green line with zero error index

915 (dotted line). **h** Mean precipitation error index versus k_{qsat} : mean error index is averaged over

916 the 7 indices in the other panels (after the signs of the 5 indices with negative best-fit slopes
917 were changed, to ensure a positive correlation with k_{qsat}).

918

919

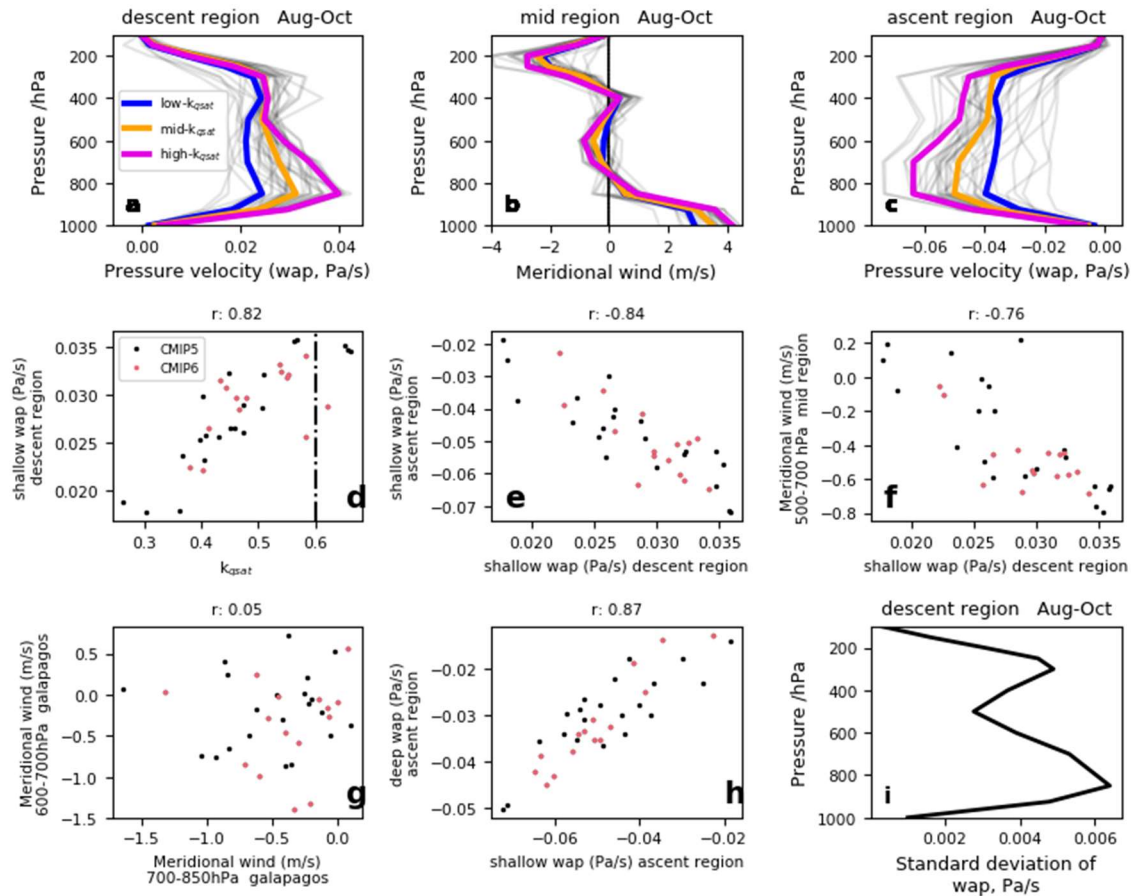


920

921 Extended data Figure 7. Supporting results for observational estimate of the $k_{q_{sat}}$ lower
 922 bound. Estimating error, from internal variability, due to the fact that the TRMM operational
 923 period only partly overlaps the time period simulated by the AMIP SST-forced models. Error
 924 magnitudes are estimated from the coupled ocean-atmosphere simulations, using differences
 925 between $k_{q_{sat}}$ estimated from all possible overlapping 17-year (TRMM-like) and 25-year
 926 (AMIP-like) periods (with the same overlap as TRMM and the 25-year SST-forced model
 927 simulations). Results are given for two methods of estimating $k_{q_{sat}}$: our ‘sortav’ method (as
 928 used throughout the manuscript), and standard OLS regression between seasonal anomalies in
 929 $\log(\text{precipitation})$ and q_{sat} .

930

931



932

933 Extended Data Figure 8. Atmospheric circulation measures in CMIP5 and CMIP6 models.

934 **a-c** thick lines are CMIP5 composite means, for (magenta) high k_{qsat} subset; (blue) low k_{qsat}

935 subset and (gold) intermediate k_{qsat} . Thin grey lines are individual models (CMIP5 and

936 CMIP6). Descent (5S-1N), mid (1-7N) and ascent (7-13N) regions are marked by vertical

937 dotted lines in Figure 5c-e. **d-h**: each symbol represents one CMIP5 (black) or CMIP6 (red)

938 model. Title gives Pearson correlation coefficient. **d** shallow descent versus k_{qsat} ; vertical line

939 marks our best estimate of k_{qsat} . **e** shallow ascent versus shallow descent. **f** shallow

940 meridional return flow versus shallow descent. **g** shallow versus very-shallow meridional

941 wind, over Galapagos: the negligible correlation indicates different physical processes at these

942 two levels. **h** deep versus shallow ascent. **i** standard deviation, across models, of the pressure

943 velocity (wap) at each pressure level.

944

945 **Extended Data Tables**

946

947

Descent region, column integrals	High k_{qsat} mean	Mid k_{qsat} mean	Low k_{qsat} mean	High k_{qsat} – Low k_{qsat}
Net radiation + sensible heat flux	-129.4	-125.9	-127.5	-1.8
Latent heating by precipitation	14.4	22.9	35.5	-21.1
Vertical advection by mean vertical velocity, integrated over 100-1000 hPa	130.1	110.0	95.5	34.6
Vertical advection by mean vertical velocity, integrated over 600-1000 hPa	74.5	57.4	48.1	26.4
Residual advection	-15.1	-7.0	-3.5	-11.6

948

949 Extended Data Table 1. Column-integrated dry static energy budget for the descent region,
 950 Aug-Oct, averaged over the high-, mid- and low- k_{qsat} groups of CMIP5 models. Vertical
 951 advection by mean vertical velocity is calculated using seasonal mean vertical velocity. The
 952 final row, calculated as a residual from the first three columns, includes horizontal advection,
 953 and vertical advection by transient eddies.

954

955

a SST dataset	Unscaled k_{qsat} estimate (no bias correction)			
HadISST	0.58			
ERSST	0.49			
COBE	0.51			
b				
SST1	SST2	K1 (X = SST1)	K2 (X = SST2)	SQRT(K1*K2)
AMIP	HadISST	0.77	1.01	0.89
AMIP	COBE	0.85	1.00	0.92
AMIP	ERSST	0.76	0.97	0.86
HadISST	COBE	0.76	0.79	0.78
HadISST	ERSST	0.83	0.55	0.68
COBE	ERSST	0.92	0.54	0.70

957

958 Extended data Table 2. Supporting results for observational estimate of the k_{qsat} lower bound
959 (see Methods for details). **a** Unscaled estimates for k_{qsat} directly estimated using TRMM
960 precipitation and three different SST datasets (the AMIP SST dataset was not used due to
961 limited temporal overlap with the TRMM operational period). These values are
962 contaminated by regression dilution bias so do not represent central estimates. **b** Estimating
963 typical values of regression dilution bias from each pair of SST datasets. K1 is the gradient
964 from linear regression when regressing SST1 against SST2 (using the sortav regression
965 method). K2 is the value obtained when regressing SST2 against SST1.

966